

**SLOVAK UNIVERSITY OF TECHNOLOGY IN BRATISLAVA**  
**Faculty of Electrical Engineering and Information Technology**

**Ing. Alen Fos**

**Dissertation Thesis Abstract**

**Crystallization kinetics and structure optimization of rapidly quenched  
Fe-Sn-B based alloys**

Reg. No.: FEI-104400-75402

**Submitted to obtain the academic title of  
„philosophiae doctor“, abbreviated as „PhD.“**

In the doctorate degree study programme:	Physical Engineering
In the field of study:	Electrical and Electronics Engineering
Form of Study:	full-time

Bratislava, May 2023

**Dissertation Thesis has been prepared at**

Institute of Physics, Slovak Academy of Sciences

**Submitter: Ing. Alen Fos**

Institute of Physics, Slovak Academy of Sciences

Dúbravská cesta 9, 845 11, Bratislava, Slovakia

**Supervisor: Ing. Peter Švec, DrSc.**

Institute of Physics, Slovak Academy of Sciences

Dúbravská cesta 9, 845 11, Bratislava, Slovakia

**Readers: prof. Ing. Marcel Miglierini, DrSc.**

Slovak University of Technology

Faculty of Electrical Engineering and Information Technology

Institute of Nuclear and Physical Engineering

Ilkovičova 3, 812 19 Bratislava, Slovakia

**doc. RNDr. Edmund Dobročka, CSc.**

Institute of Electrical Engineering, Slovak Academy of Sciences

Dúbravská cesta 9, 841 04, Bratislava, Slovakia

Dissertation Thesis Abstract was sent .....

Dissertation Thesis Defence will be held on .....

at Institute of Physics, Slovak Academy of Sciences, Dúbravská cesta 9, 845 11, Bratislava

**prof. Ing. Vladimír Kutiš, PhD.**

Dean of FEI STU

# Contents

1	Introduction .....	1
2	Goals of the dissertation thesis .....	2
3	Nominal chemical composition of selected systems .....	3
4	Experimental methods .....	4
5	Results and discussion .....	5
5.1	Thermal analysis of Fe-Sn-B system .....	6
5.2	Structural analysis of Fe-Sn-B systems.....	14
5.3	Magnetic properties.....	30
6	Conclusion .....	34
7	Záver.....	36
8	References .....	38
9	List of publications .....	41

# 1 Introduction

Ternary Fe-Sn-B system was studied for the first time by Dunlap in 1982 [1], where it was reported that amorphous ribbons of 20  $\mu\text{m}$  thickness were obtained in the compositions  $\text{Fe}_{79}\text{Sn}_1\text{B}_{20}$  and  $\text{Fe}_{78}\text{Sn}_2\text{B}_{20}$ . Later Battezzati et al. [2] studied the kinetics of formation and thermal stability of Fe-X-B metallic glasses and reported that  $\text{Fe}_{82}\text{Sn}_{1.5}\text{B}_{16.5}$  amorphous ribbons with a 20  $\mu\text{m}$  thickness could be obtained by means of the single roller technique. They concluded that metallic glasses which are more difficult to prepare by liquid quenching are often the more resistant to crystallization. Arconado et al. [3] studied glass forming tendency in the Fe-Sn-B system. They produced amorphous ribbons with a 20  $\mu\text{m}$  and 40  $\mu\text{m}$  thickness with various amount of Sn. Sample with highest amount of Sn that was successfully produced in amorphous state had chemical composition  $\text{Fe}_{84}\text{Sn}_4\text{B}_{12}$  and was 20  $\mu\text{m}$  thick.

Recently Illekova [4] and Matko [5] studied crystallization behavior and microstructure of amorphous  $\text{Fe}_{95-x}\text{Sn}_5\text{B}_x$  ( $x = 15, 17, 20$ ) alloys in form of the ribbons. They found that Sn atoms most probably substitute some of Fe atoms in emerging Fe-bcc structure. Presence of Sn results in very intense nucleation and growth of the grains rapidly decays.

Hyperfine interactions in alloys of same composition as in [4] and [5] was studied by Miglierini and Rusakov [6] using  $^{57}\text{Fe}$  and  $^{119}\text{Sn}$  Mössbauer spectrometry at room temperature. Being able to use two resonant nuclei in ternary system gives access to closer examination of hyperfine parameters especially for amorphous phase. They found that even absolute values of spectral parameters were different, similar trends in behavior with increase in annealing temperature were observed for both resonant nuclei. Relative contents of amorphous and crystalline phases were very similar from point of view of both resonant nuclei.

Effect of the addition of Sn to Fe-B-P alloys on magnetic properties was studied by Li et al. [7]. They found that saturated magnetic flux density gradually increases with addition of Sn.  $B_s$  of about 1.6 T and  $H_c$  of about 5 A/m were achieved. Small addition (just 0.5 atomic percent) of Sn to Fe-B-C-Si-P reduces  $H_c$  from 14 A/m to 6.6 A/m while maintaining  $B_s$  about 1.7 T. Addition of Co increases  $B_s$  and  $T_c$  but decreases  $H_c$ . By addition of Sn to Fe-Co-B-C-Si-P alloys,  $H_c$  decreases from 29.5 A/m to 12.4 A/m [8].

Preliminary results of  $\text{Fe}_{81}\text{Sn}_7\text{B}_{12}$  and  $\text{Fe}_{78}\text{Sn}_7\text{B}_{15}$  rapidly quenched alloys were published in 2016 [9]. These results were to best of our knowledge first reported case of Fe-Sn-B based ribbons with 7 atomic percent of Sn in amorphous state. There was one study that reported Fe-Sn-B alloy in amorphous state with 13.3, 17.4, 23 and 26.9 at. % of Sn but these samples were prepared by reducing iron and tin salts with  $\text{KBH}_4$  in an aqueous solution [10].

At the time when we started working on a project that resulted in my diploma thesis and subsequently in this dissertation thesis the above-mentioned publications were to the best of our knowledge the only publications mentioning Fe-Sn-B based rapidly quenched alloys.

## **2 Goals of the dissertation thesis**

Taking into consideration state of the literature, we defined aims of the presented thesis in the following points:

- Preparation of Fe-Sn-B based rapidly quenched alloys with enhanced amount of Sn by planar flow casting and optimization of preparation process.
- Analysis of crystallization kinetics of prepared alloys during transformation from metastable state to nanocrystalline phases using differential scanning calorimetry and resistometry.
- Study of microstructure and morphology of prepared alloys in various states of crystallization process in as-quenched state as well as after various types thermal treatment using x-ray diffraction and transmission electron microscopy. Determination of the effect of different types of thermal treatments on microstructure and morphology of prepared samples in order to obtain information about phase transformation.
- Measurements of selected magnetic properties, especially hysteresis curves and Curie temperatures by vibrating sample magnetometer and magnetic thermogravimetry.
- Optimization of thermal treatment of selected systems with the aim to improve magnetic properties.
- Determination of the effect of additional elements on structure and magnetic properties of samples.

### 3 Nominal chemical composition of selected systems

When designing chemical composition for soft magnetic system with high  $B_s$ , we tried to maximize amount of ferromagnetic element (Fe and Co) while keeping amount of glass forming element (B) minimal but sufficient for formation of amorphous structure. Sn was used as both nucleation enhancer and as grain growth inhibitor. The amount of ferromagnetic element varied from 78 at. % to 83 at. % while amount of glass forming element varied from 12 at. % to 15 at. %; the amount of Sn was either 5 at. % or 7 at. %. Enhanced amount of Sn is close to the limit of Sn solubility in Fe. Sn does not readily dissolve in Fe, except for elevated temperatures, and forms no solid solution with boron [11]. It was reported that addition of Co to Fe-based alloys results in increase of  $T_c$  and in most cases also of  $B_s$  [12], [13], [14]. This motivated us to try Co/Fe substitution (ratio was Fe : Co = 3 : 1) and addition of small amount of Cu which has potential to refine structure. Nominal chemical compositions of prepared alloys are listed in Table 3.1.

Table 3.1: List of nominal chemical compositions of master alloys and consequently rapidly quenched ribbons.

Base composition	Addition of Co	Addition of Cu	Addition of Co and Cu
$\text{Fe}_{78}\text{Sn}_7\text{B}_{15}$	$(\text{Fe}_3\text{Co}_1)_{78}\text{Sn}_7\text{B}_{15}$	$(\text{Fe}_{78}\text{Sn}_7\text{B}_{15})_{99}\text{Cu}_1$	$((\text{Fe}_3\text{Co}_1)_{78}\text{Sn}_7\text{B}_{15})_{99}\text{Cu}_1$
$\text{Fe}_{81}\text{Sn}_7\text{B}_{12}$	$(\text{Fe}_3\text{Co}_1)_{81}\text{Sn}_7\text{B}_{12}$	$(\text{Fe}_{81}\text{Sn}_7\text{B}_{12})_{99}\text{Cu}_1$	$((\text{Fe}_3\text{Co}_1)_{81}\text{Sn}_7\text{B}_{12})_{99}\text{Cu}_1$
$\text{Fe}_{83}\text{Sn}_5\text{B}_{12}$	$(\text{Fe}_3\text{Co}_1)_{83}\text{Sn}_5\text{B}_{12}$	$(\text{Fe}_{83}\text{Sn}_5\text{B}_{12})_{99}\text{Cu}_1$	$((\text{Fe}_3\text{Co}_1)_{83}\text{Sn}_5\text{B}_{12})_{99}\text{Cu}_1$

All studied systems that are subjects of this thesis were prepared at Institute of Physics, Slovak Academy of Sciences. Master alloy ingots with nominal chemical composition were prepared by melting pure elements (purity > 99.9 %) in an induction furnace. Final samples in the form of ribbons were prepared by planar flow casting from master alloy ingots. Ribbons were approximately 20  $\mu\text{m}$  thick and 3 mm or 6 mm wide.

## 4 Experimental methods

Prepared samples were analyzed by various experimental methods which are available at Institute of Physics, Slovak Academy of Sciences in Bratislava and Institute of Nuclear and Physical Engineering, Faculty of Electrical Engineering and Information Technology of Slovak University of Technology in Bratislava. Exception were magnetic hysteresis loops measurements which were done at Institute of Experimental Physics, Slovak Academy of Sciences in Košice.

Samples in as-quenched state were annealed isothermally and in linear heating regime to study changes in microstructure and in magnetic properties. Thermal treatment was performed in furnace constructed for thermal treatment and resistometry measurements of ribbon shaped samples. Outer region of the furnace can be evacuated which gives us the option to thermally treat ribbons in air atmosphere, in vacuum and in argon atmosphere. Samples can be put in and out of the furnace in less than 5 s. Electrical resistivity of samples was measured by four-point technique.

Crystallization kinetics of as-quenched ribbons was analyzed with power compensated differential scanning calorimeter DSC 7 by Perkin Elmer. Ribbons were cut into pieces and encapsulated into aluminum pan. Typical weight of encapsulated material was around 10 mg.

Magnetic thermogravimetry measurements was used to determine Curie temperature ( $T_c$ ) of amorphous and crystal phases in the studied material. Measured sample is placed in a magnetic field created by permanent magnet (20 mT) and at certain temperature close to  $T_c$ , analyzer detects changes (decrease) in weight. Measured weight is sum of actual weight and magnetic force. Changes in magnetic force due to phase transition is detected. Result of thermogravimetric analysis (TGA) measurement is called TGA curve [15]. Thermogravimetric analyzer used for magnetic thermogravimetry measurements was TGA 7 by Perkin Elmer.

Phase analysis was done by x-ray diffraction (XRD) at room temperature. X-ray diffractometer used for qualitative analysis of studied samples was Bruker D8 Advance with Cu  $K_\alpha$  radiation ( $\lambda = 0.154056$  nm) and scintillation counter type detector in parallel beam configuration. A Göbel mirror and  $K_\beta$  filter were installed in the incident beam and a  $0.23^\circ$  Soller slit and LiF monochromator in the diffracted beam path. X-ray diffractometer used for quantitative analysis of studied samples was Bruker D8 Advance with Bragg-Brentano geometry using Co  $K_\alpha$

radiation. Diffractograms were collected in the range of  $2\theta$  angles from  $20^\circ$  to  $130^\circ$  with  $0.025^\circ$  step and with typical collection time per step 2.5 s. X-axis of diffractograms collected using Co  $K\alpha$  radiation was recalculated to Cu  $K\alpha$  radiation for better comparison.

Morphology of samples was examined by transmission electron microscope (TEM) JEOL JEM-2000FX at 200 kV. Images both in bright field and in dark field were taken using adapted Erlangshen ES500W CCD camera (GATAN). Samples for TEM were cut in the form of disc with 3 mm diameter and thinned by precision ion polishing system PIPS 691 (GATAN) using Ar ions for sample thinning.

Mössbauer spectrometry measurements were performed in transmission geometry at room temperature. Source of  $\gamma$ -rays from  $^{57}\text{Co}$  atoms embedded in Rh matrix was placed on solenoid moving towards and away from the measured sample with constant acceleration. Photons emitted from measured sample were detected with NaI(Tl) scintillation detector.

Magnetic hysteresis loops of selected studied systems in as-quenched state and after thermal treatment was measured using MicroSense EV9 vibrating sample magnetometer (VSM) at room temperature. Magnetic field was applied in the longitudinal direction of the ribbon.

## 5 Results and discussion

As-quenched state of samples was checked by XRD. To achieve amorphous structure of ribbon, it is necessary to optimize production parameters such as temperature of the melt, rotation speed of copper wheel, etc. Diffractograms of as-quenched ribbons are shown in Figure 5.1. For each chemical composition, multiple ribbons were produced with different production parameters. Ribbons with best mechanical properties in combination with amorphous structure (or at least closest to amorphous structure) were used in further study. Samples without Cu in as-quenched state exhibit only broad peaks typical for amorphous structure. Samples with Cu addition were more difficult to produce in amorphous state, as can be seen by comparison of Figure 5.1 (a) and (b). Crystalline phases that occur in partially crystalline ribbons were identified as  $\alpha$ -Fe with body centered structure and  $\text{Fe}_2\text{Sn}$  with hexagonal structure.

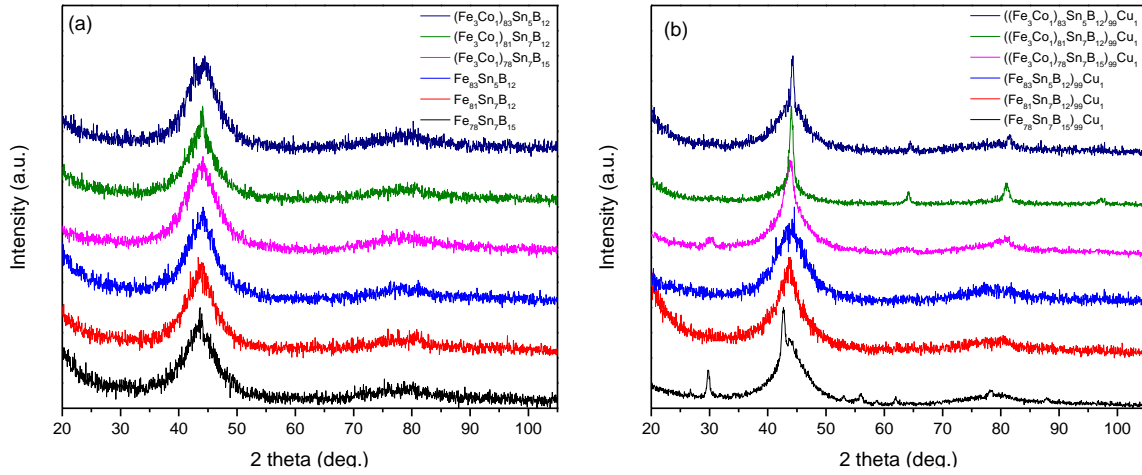


Figure 5.1: Diffractograms of as-quenched ribbons without addition of Cu (a) and with addition of Cu (b). Individual traces are shifted vertically for clarity.

## 5.1 Thermal analysis of Fe-Sn-B system

Investigated alloys exhibit two stages of crystallization R1 and R2 which is visible in Figure 5.2. Addition of Cu decreases onset temperature of the first stage of crystallization. Addition of Co increases both  $T_{x1}$  and  $T_{x2}$ . Samples with lower amount of B (12 at. % vs 15 at. %) exhibit lower  $T_{x1}$  but  $T_{x2}$  remains unchanged. Changing amount of Sn (5 at. % vs 7 at. %) does not have significant effect on transformation temperatures. Comparison between DSC and resistometry signal of  $\text{Fe}_{81}\text{Sn}_7\text{B}_{12}$  system recorded at heating rate of 10 K/min is shown in Figure 5.3. Both first and second stage of crystallization caused decrease of electrical resistivity of measured sample and clear correlation with DSC signal is visible.

Isothermal crystallization of  $\text{Fe}_{81}\text{Sn}_7\text{B}_{12}$  system was followed by resistometry measurements shown in Figure 5.4. Decrease of electrical resistivity caused by first stage of crystallization starts after less than 1 min of thermal processing. Increase of annealing temperature shifts curves to the left. Annealing at temperatures from 598 K up to 673 K does not activate second stage of crystallization even after 2 h of annealing. Increase of annealing temperature up to 723 K and 748 K successfully activated second stage of crystallization after 10 min and 1 min of annealing, respectively. These results are very useful for selecting annealing parameters of samples for structure analysis.

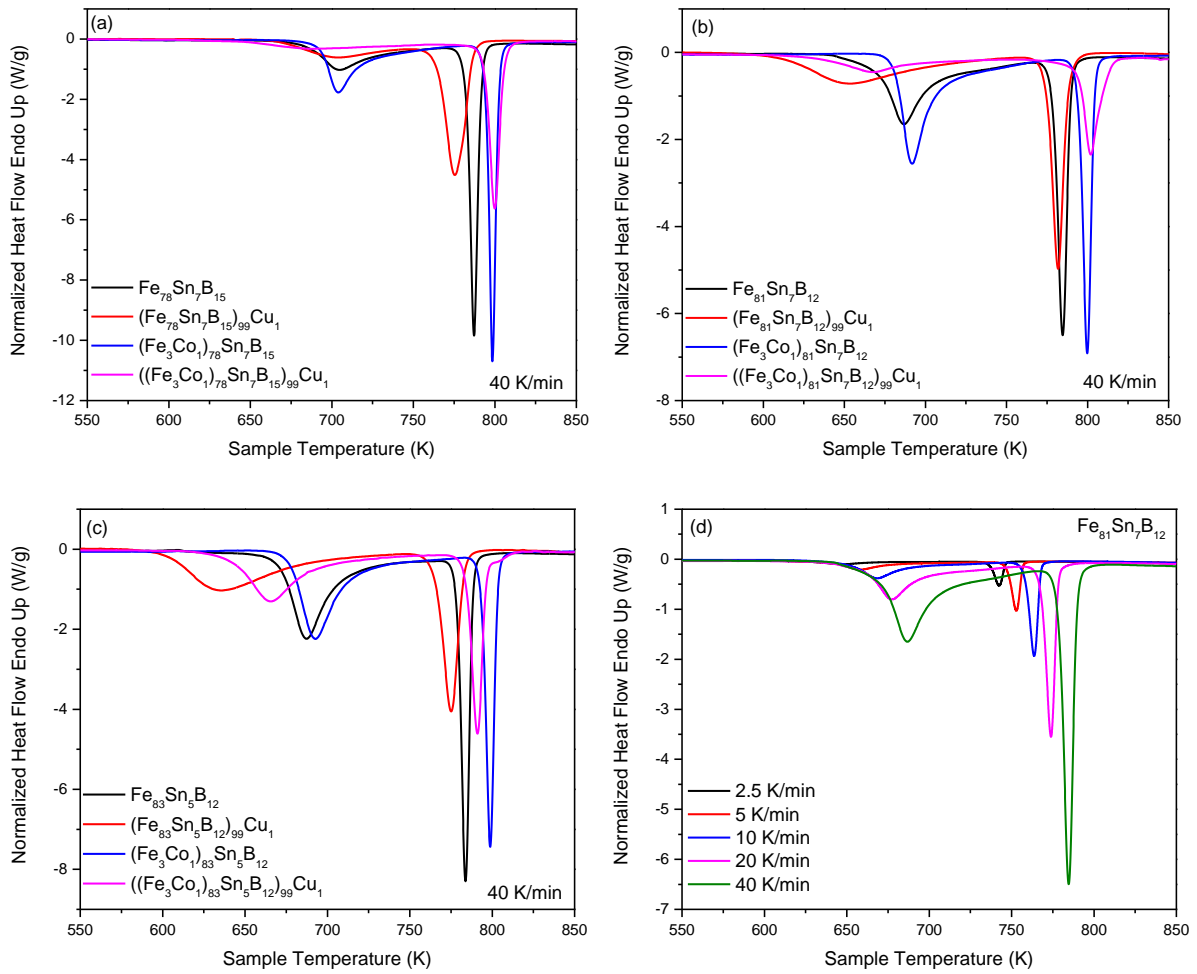


Figure 5.2: DSC linear-heating curves recorded at heating rate of 40 K/min of as-quenched systems with (a) 78 at. % of ferromagnetic elements, (b) 81 at. % of ferromagnetic elements, (c) 83 at. % of ferromagnetic elements and (d) DSC curves of as-quenched system with 81 at. % of Fe recorded at different heating rates noted in graph.

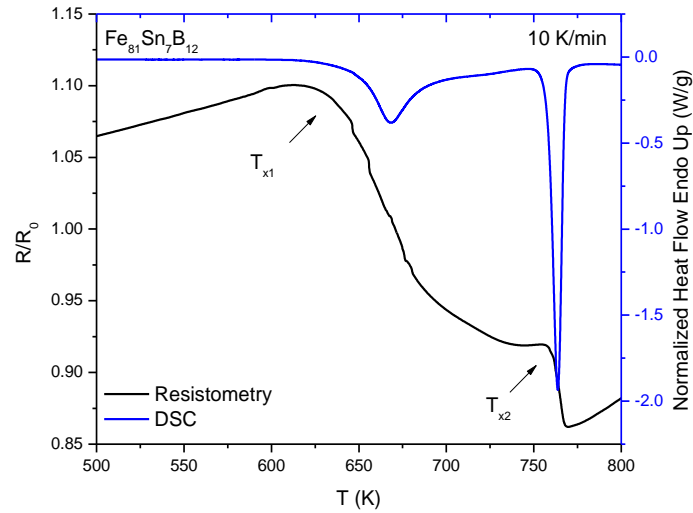


Figure 5.3: Comparison between DSC and resistometry signal of  $\text{Fe}_{81}\text{Sn}_7\text{B}_{12}$  system recorded at heating rate of 10 K/min. Resistometry signal was normalized to value at the beginning of the measurement.

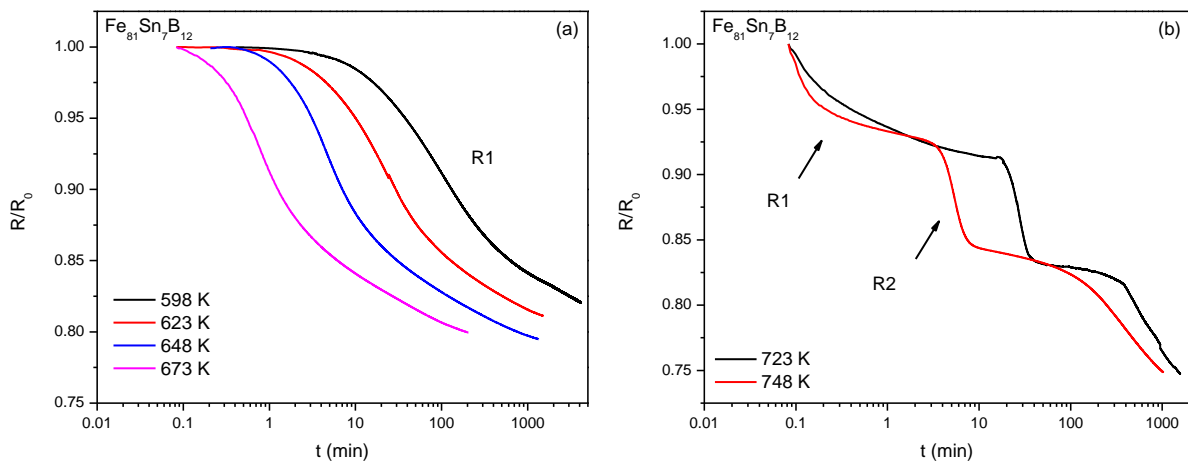


Figure 5.4: Isothermal resistivity measurements of  $\text{Fe}_{81}\text{Sn}_7\text{B}_{12}$  system at selected temperatures that activate (a) first R1 and (b) second R2 stage of crystallization. Resistometry signal was normalized to value at the beginning of the measurement.

Johnson-Mehl-Avrami-Kolmogorov (JMAK) model is used to describe crystallization kinetics of wide variety of materials including rapidly quenched alloys [16] [17] [18]. Kissinger equation was used to determine activation energies of both the first and the second stages of crystallization [19]. Results are shown in Figure 5.5.

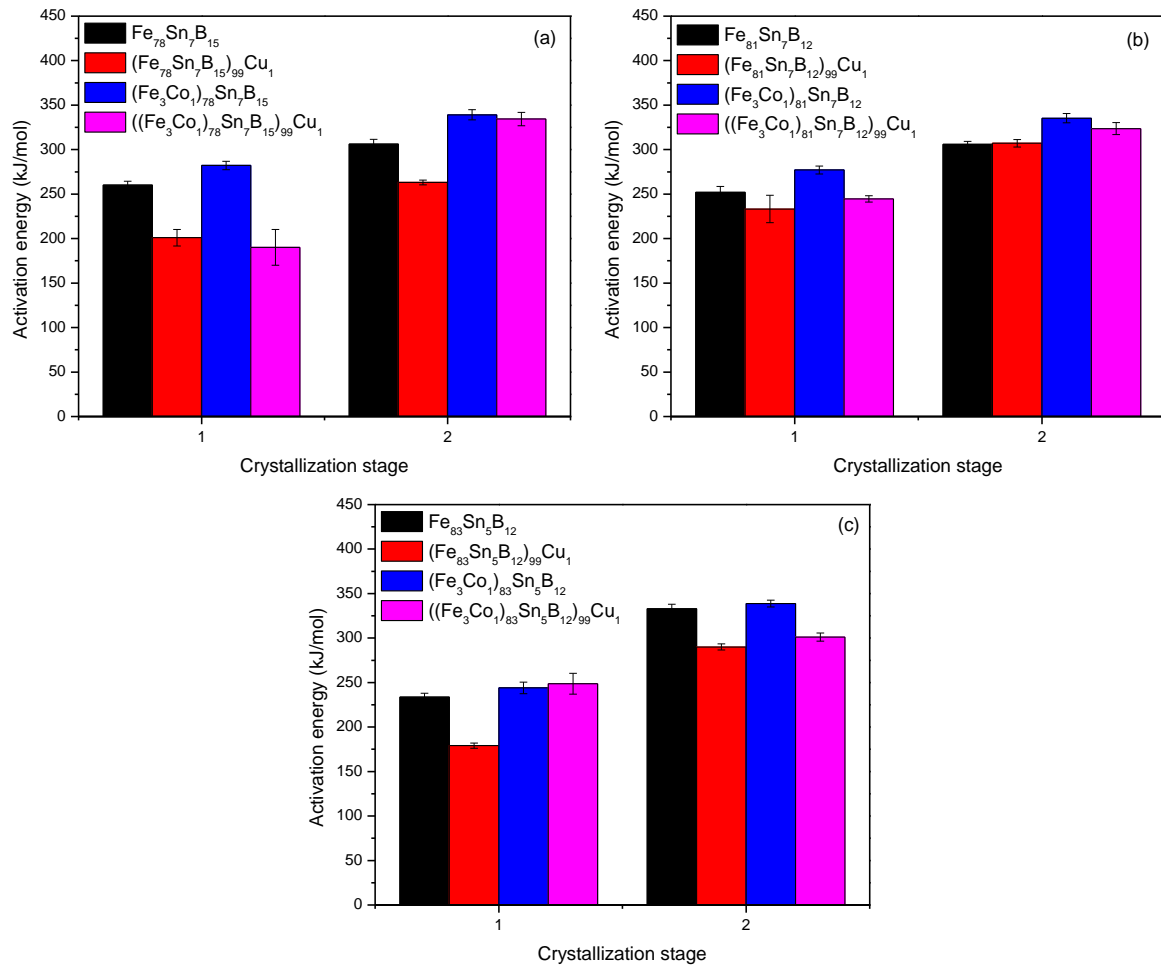


Figure 5.5: Calculated activation energies (a), (b), (c) for both the first R1 and the second R2 stage of crystallization of studied systems with 78 at. % of ferromagnetic elements, 81 at. % of ferromagnetic elements and 83 at. % of ferromagnetic elements, respectively.

Addition of Cu decreases value of activation energy for the first stage of crystallization to but does not affect the second stage of crystallization, while addition of Co increases activation energies for both the first and the second stage of crystallization. Increase of amount of B increases activation energy of first stage of crystallization but does not influence value of  $E_2$ . Increase of amount of Sn increases activation energy of first stage of crystallization and decreases value of  $E_2$ .

Activation energy calculated with Kissinger method in Figure 5.5 represents value at maximum rate of conversion which does not have to be constant throughout whole reaction. Kissinger-Akahira-Sunose (KAS) equation was used to calculate local activation energy at various extents of conversion  $E(\alpha)$  [20]. Local activation energy as a function of extent of conversion of selected systems is shown in Figure 5.6.

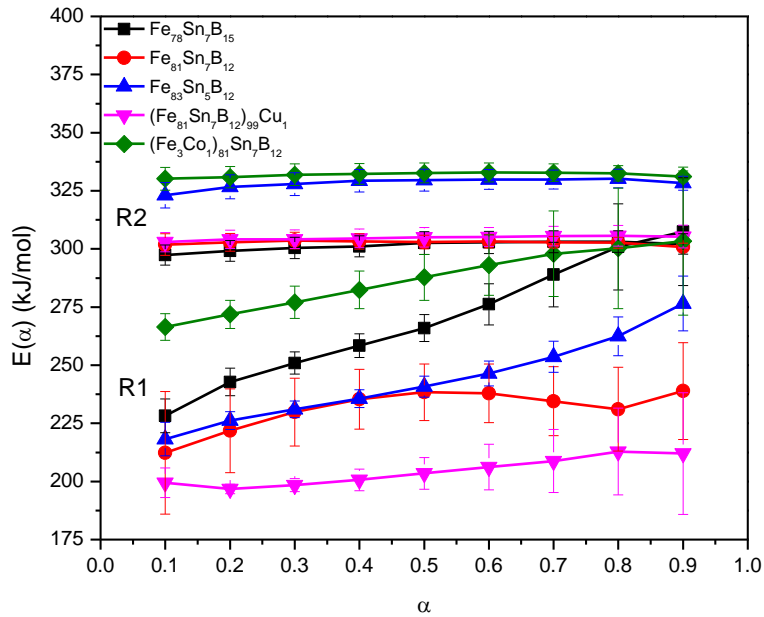
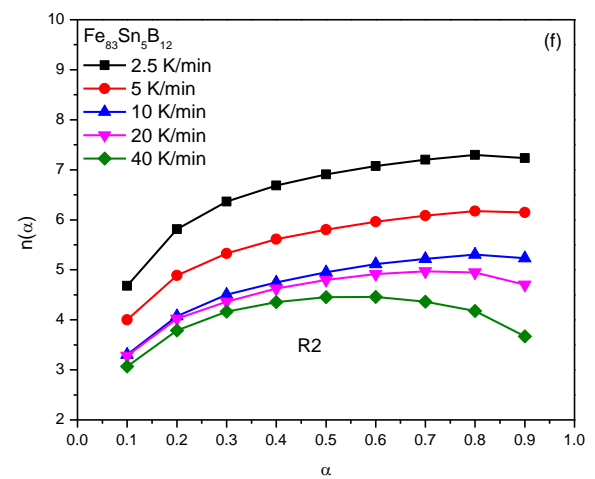
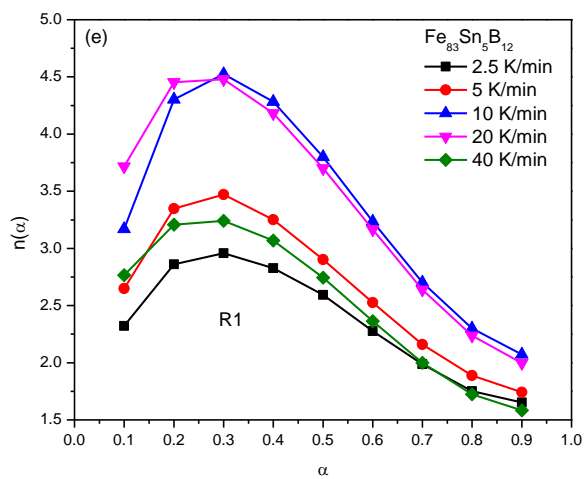
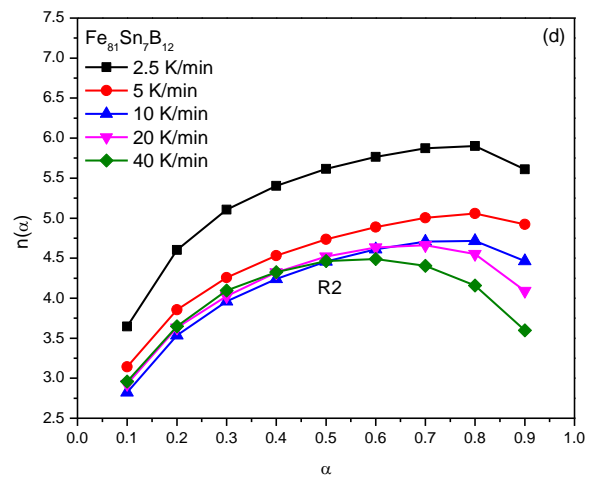
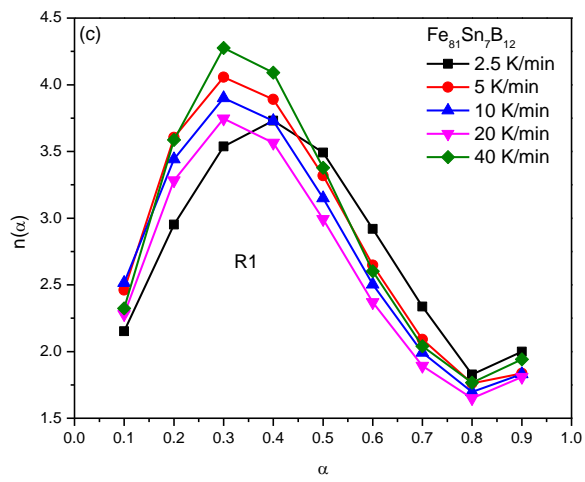
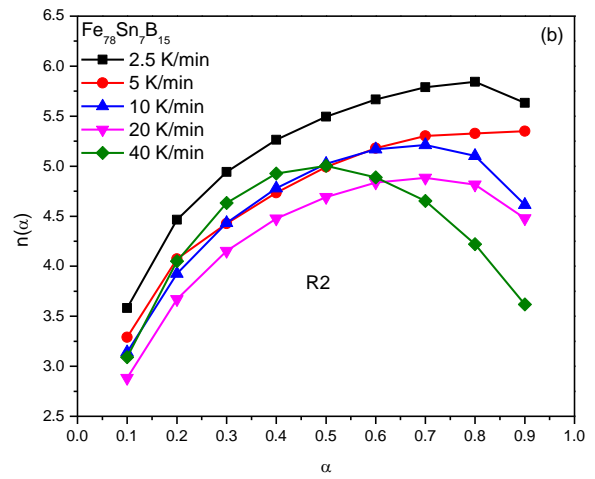
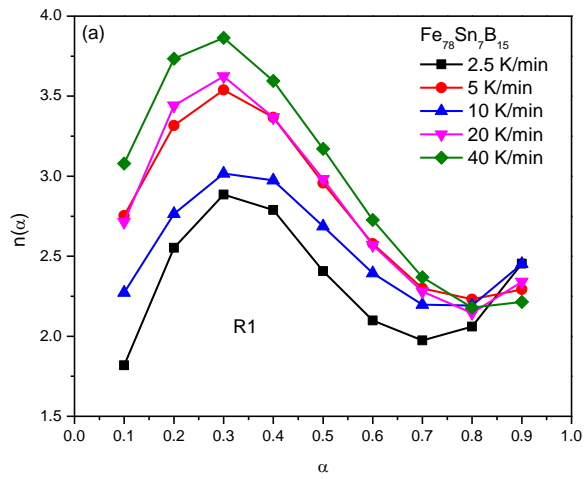


Figure 5.6: Dependence of local activation energy on the extent of conversion of  $\text{Fe}_{78}\text{Sn}_7\text{B}_{15}$ ,  $\text{Fe}_{81}\text{Sn}_7\text{B}_{12}$ ,  $\text{Fe}_{83}\text{Sn}_5\text{B}_{12}$ ,  $(\text{Fe}_{81}\text{Sn}_7\text{B}_{12})_{99}\text{Cu}_1$  and  $(\text{Fe}_3\text{Co}_1)_{81}\text{Sn}_7\text{B}_{12}$  systems for both the first R1 and the second R2 stage of crystallization.

Local activation energy follows similar trend as activation energy at maximum rate of crystallization which for the first stage of crystallization increases with increase in amount of B, decreases with addition of Cu and increases with addition of Co. For the second stage of the crystallization, variation in amount of B does not influence local activation energy. Decrease of amount of Sn increases local activation energy. Addition of Cu does not influence local activation energy, while addition of Co increases local activation energy for the second stage of the crystallization.

Another valuable parameter for understanding crystallization kinetics is Avrami exponent  $n$  which is used to define mechanism of nucleation and growth of crystals during crystallization process. Calculated values of local Avrami exponent  $n(\alpha)$  as a function of extent of conversion  $\alpha$  for both the first and the second stage of crystallization of selected systems are shown in Figure 5.7. Local Avrami exponent was calculated for every heating rate and from results in Figure 5.7 its can be concluded that  $n(\alpha)$  does not show clear trend in respect to change in heating rate. For both the first and the second stage of crystallization local Avrami exponent increases at the beginning of reaction and decreases with increase of  $\alpha$ .



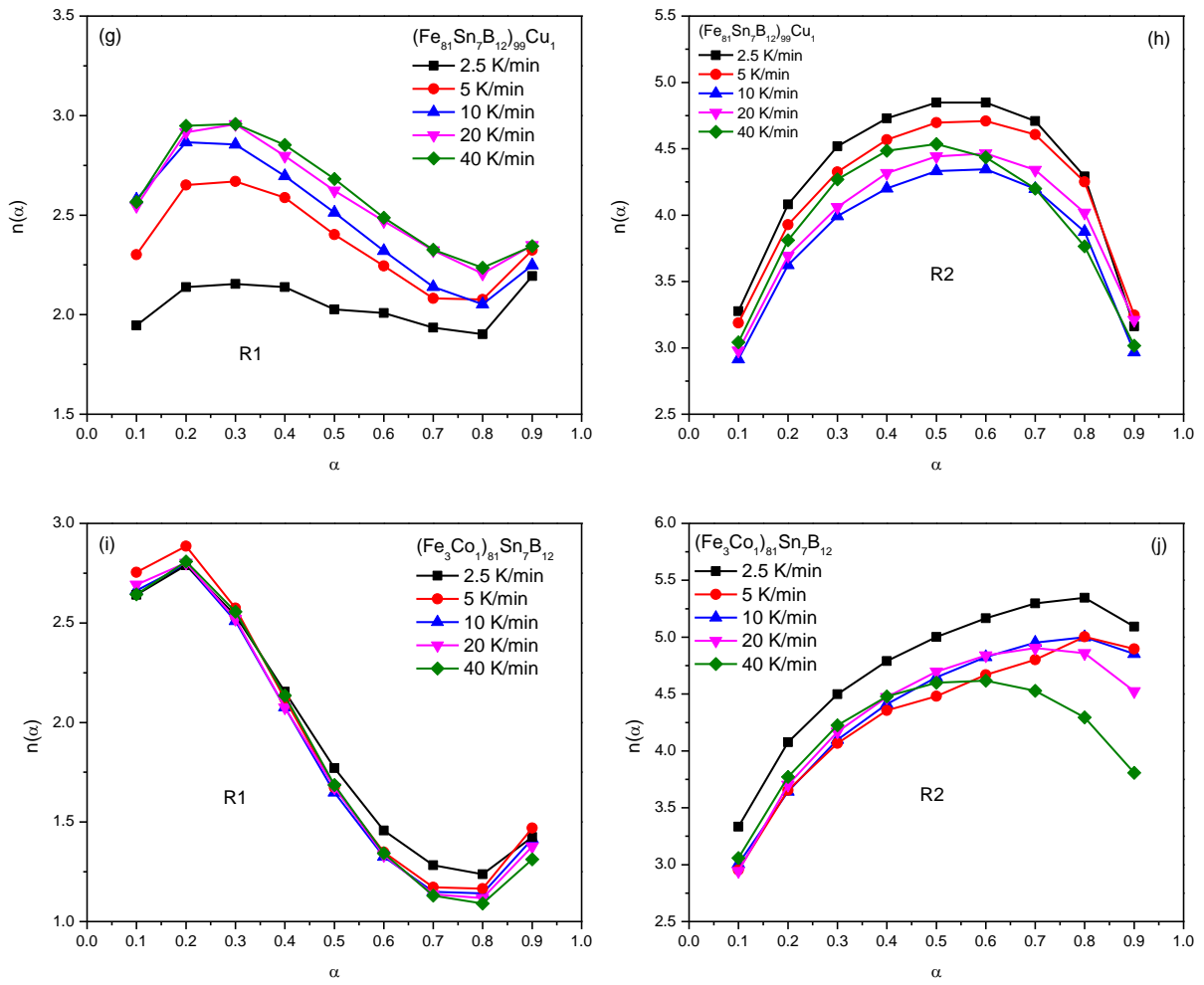


Figure 5.7: Local Avrami exponents  $n(\alpha)$  as a function of extent of conversion  $\alpha$  for  $\text{Fe}_{78}\text{Sn}_7\text{B}_{15}$  the first (a) and the second (b) stage of crystallization.  $\text{Fe}_{81}\text{Sn}_7\text{B}_{12}$  the first (c) and the second (d) stage of crystallization.  $\text{Fe}_{83}\text{Sn}_5\text{B}_{12}$  the first (e) and the second (f) stage of crystallization.  $(\text{Fe}_{81}\text{Sn}_7\text{B}_{12})_{99}\text{Cu}_1$  the first (g) and the second (h) stage of crystallization, and  $(\text{Fe}_3\text{Co}_1)_{81}\text{Sn}_7\text{B}_{12}$  the first (i) and the second (j) stage of crystallization recorded at indicated heating rates.

Calculated results of local activation energy and local Avrami exponents were verified by calculating theoretical extent of conversion using equation as described in [21] and [22]. Comparison of experimental and simulated conversion curves for  $\text{Fe}_{78}\text{Sn}_7\text{B}_{15}$  alloy is shown in Figure 5.8. Calculated and measured values are in good agreement.

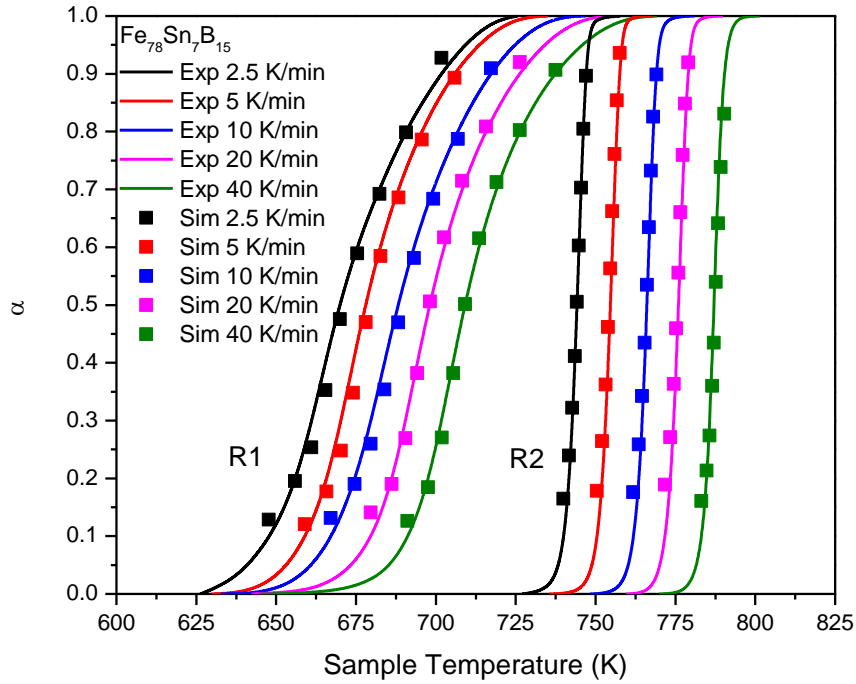


Figure 5.8: Comparison of experimental (lines) and simulated (points) conversion curves of both R1 and R2 reactions for  $\text{Fe}_{78}\text{Sn}_7\text{B}_{15}$  system recorded at different heating rates noted in graph.

Avrami exponent can be deconstructed in following way  $n = a + b \cdot p$  as proposed in [23], where  $a$ , is called nucleation index,  $b$  is dimensionality of growth, and  $p$  is growth index. Crystallization process of Fe-based amorphous alloys has been extensively reported to be three dimensional and controlled by diffusion which means that value of dimensionality of growth  $b = 3$  and value of growth index  $p = 0.5$  [24] [25]. Considering the fact that  $b = 3$  and  $p = 0.5$ , possible values of Avrami exponent are reduced to values in Table 5.1.

Table 5.1: Values of Avrami exponent in case of crystallization controlled by diffusion, which is the case of Fe-based amorphous alloys

Parameter	Value	Interpretation
n	<1.5	Growth of pre-existing nuclei
	1.5	Growth with zero nucleation rate
	(1.5,2.5)	Growth with decreasing nucleation rate
	2.5	Growth with constant nucleation rate
	>2.5	Growth with increasing nucleation rate

Considering Table 5.1 crystallization mechanism of studied alloys could be considered as growth with increasing nucleation rate for the second stage of crystallization R2 in case of all selected systems. It can be assumed that crystallization mechanism of the first stage of crystallization for  $\text{Fe}_{78}\text{Sn}_7\text{B}_{15}$ ,  $\text{Fe}_{81}\text{Sn}_7\text{B}_{12}$ ,  $\text{Fe}_{83}\text{Sn}_5\text{B}_{12}$  and  $(\text{Fe}_{81}\text{Sn}_7\text{B}_{12})_{99}\text{Cu}_1$  systems started as growth with increasing nucleation rate to  $\alpha = 0.5$  after which it continued as growth with decreasing nucleation rate. On the other hand, crystallization mechanism of  $(\text{Fe}_3\text{Co}_1)_{81}\text{Sn}_7\text{B}_{12}$  system could be proposed as a growth with increasing nucleation rate at  $\alpha = 0.1$  at the beginning of the reaction. Then it changes into growth with decreasing nucleation rate between  $\alpha = 0.3$  and  $\alpha = 0.5$ , finally, after  $\alpha = 0.5$  nucleation rate decreases to zero and rest of crystallization stage is governed by growth of already existing nuclei.

It has to be kept in mind that proposed mechanism of crystallization assumes three dimensional growth controlled by diffusion. Another valuable detail that should be kept in mind is that values of Avrami exponent are influenced by choice of  $T_0$ , starting temperature of exothermic peak which was chosen at  $\alpha = 0.5$  %. Therefore, values of Avrami exponent should be considered as an indication of proposed crystallization mechanism and as a starting point for subsequent research.

## 5.2 Structural analysis of Fe-Sn-B systems

Studied alloys were annealed isothermally at selected temperatures for selected time interval (30 min) sufficient to activate first stage of crystallization but insufficient to activate second stage of crystallization. Diffractograms of studied alloys after thermal treatment are shown in Figure 5.9. In first stage of crystallization of all studied alloys,  $\alpha$ -Fe phase with bcc structure crystallizes from amorphous matrix. XRD pattern of  $(\text{Fe}_{78}\text{Sn}_7\text{B}_{12})_{99}\text{Cu}_1$  alloy exhibits in addition to  $\alpha$ -Fe phase also  $\text{Fe}_2\text{Sn}$  phase which was present in as-quenched sample.

Bright field and dark field TEM micrographs of selected alloys in as-quenched state as well as corresponding selected area electron diffraction (SAED) patterns are shown in Figures 5.10. Base compositions  $\text{Fe}_{78}\text{Sn}_7\text{B}_{15}$  and  $\text{Fe}_{81}\text{Sn}_7\text{B}_{12}$  in as-quenched state shown in Figure 5.10 (a) and (b) exhibits fully amorphous structure which is confirmed by corresponding SAED pattern that shows just diffuse halo rings, in accord with the corresponding XRD pattern shown in Figure 5.1. Addition of Cu decreases glass forming ability of the alloys which results in

presence of  $\alpha$ -Fe grains embedded in amorphous matrix of samples in as-quenched state shown in Figure 5.10 (c) and (d). Corresponding SAED pattern shows diffuse halo rings with few bright spots that correspond to  $\alpha$ -Fe grains.

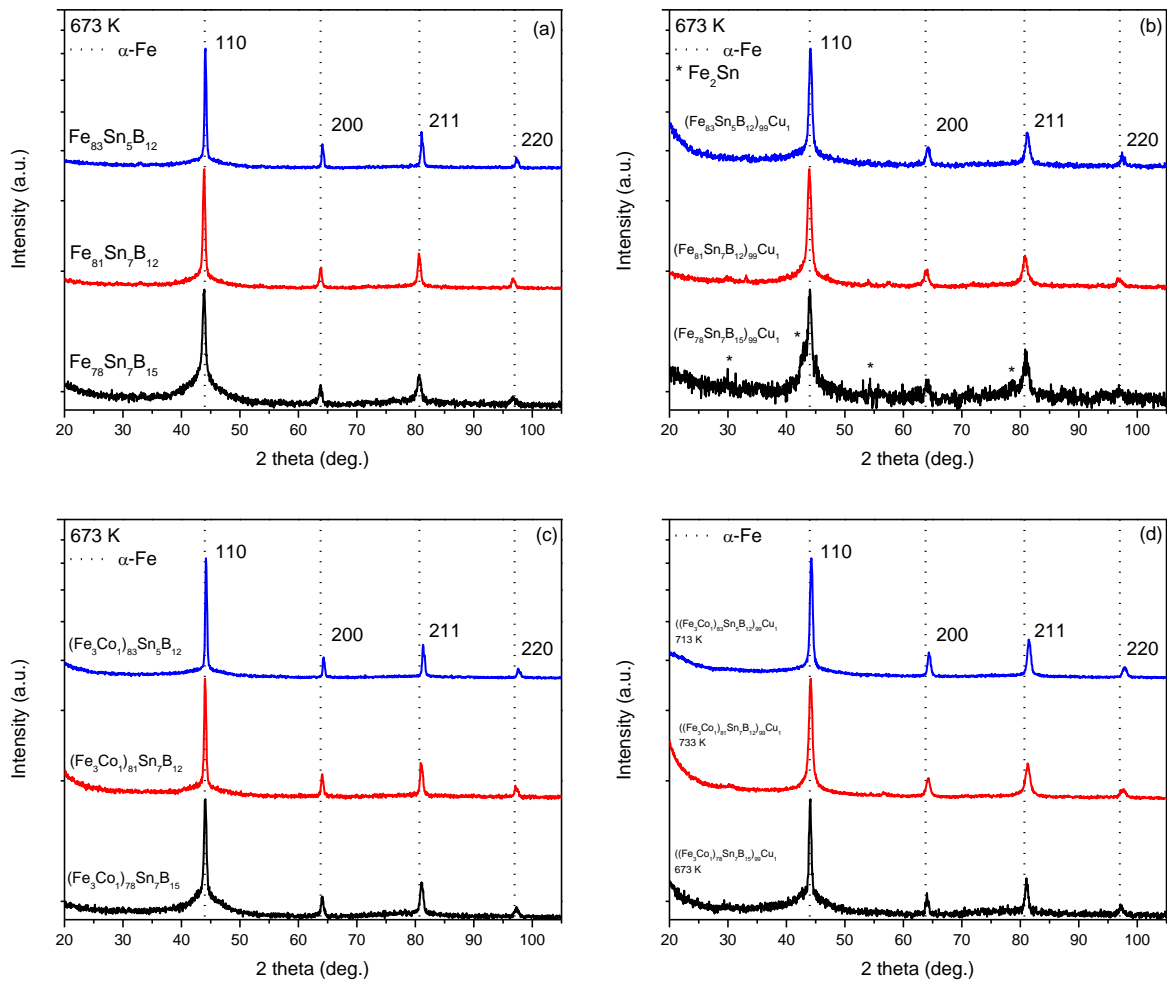


Figure 5.9: XRD patterns of (a) base compositions, (b) alloys with addition of Cu, (c) alloys with addition of Co and (d) alloys with addition of both Cu and Co. Samples after isothermal annealing at indicated temperature for 30 min. Identified phases are listed. Peaks corresponding to individual family of lattice planes are indicated with vertical dotted lines and corresponding Miller indices in case of  $\alpha$ -Fe. Peaks that correspond to  $\text{Fe}_2\text{Sn}$  phase are indicated with symbols. Individual traces are shifted vertically for clarity.

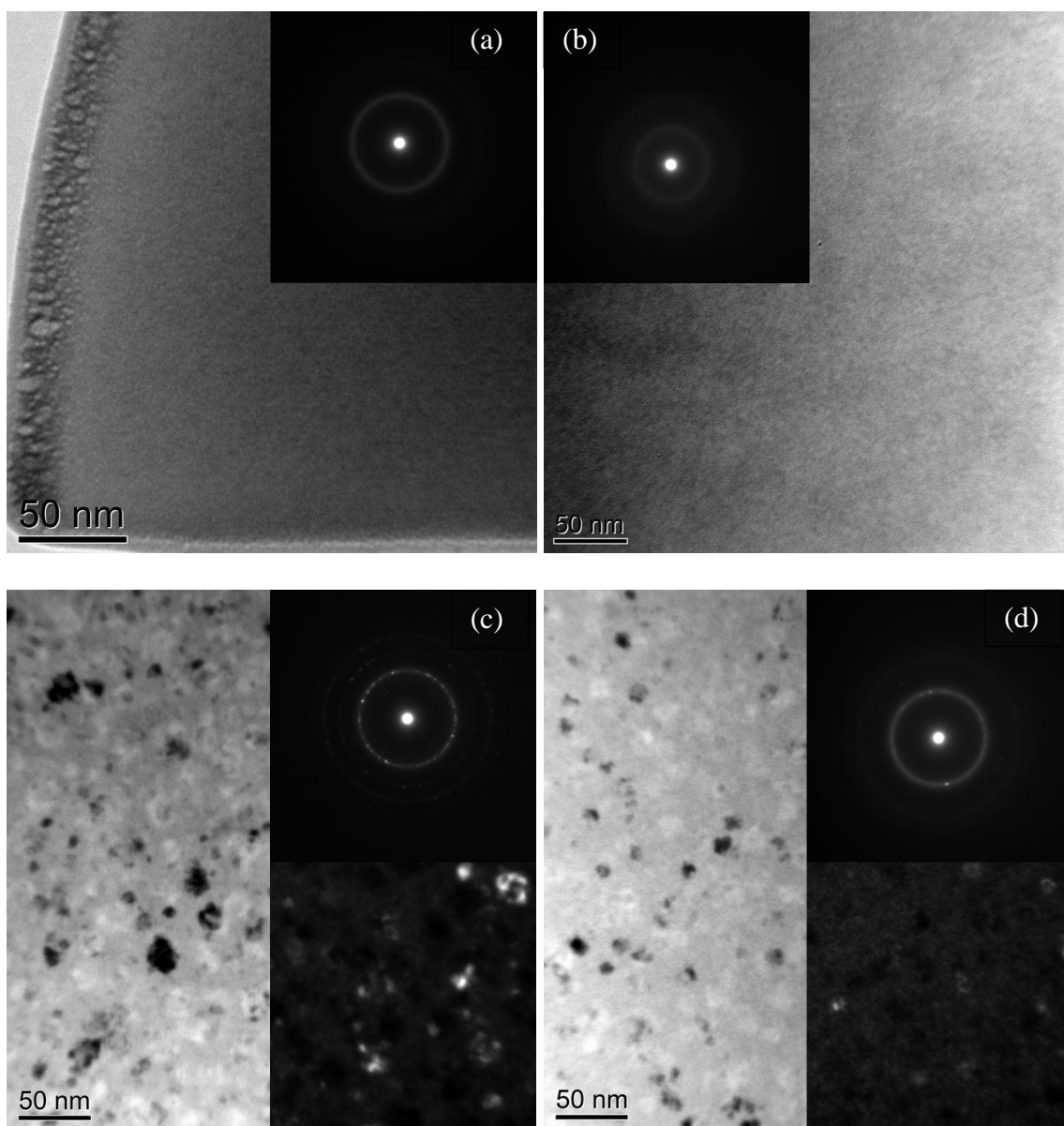


Figure 5.10: Bright field and dark field TEM images and corresponding SAED patterns of (a)  $\text{Fe}_{78}\text{Sn}_7\text{B}_{15}$ , (b)  $\text{Fe}_{81}\text{Sn}_7\text{B}_{12}$ , (c)  $((\text{Fe}_3\text{Co}_1)_{78}\text{Sn}_7\text{B}_{15})_{99}\text{Cu}_1$  and (d)  $(\text{Fe}_{81}\text{Sn}_7\text{B}_{12})_{99}\text{Cu}_1$  in as-quenched state.

Morphology of selected systems after thermal treatment sufficient to activate first stage of crystallization but insufficient to activate second stage of crystallization is shown in Figure 5.13, bright field and dark field TEM micrographs with SEAD patterns are shown.

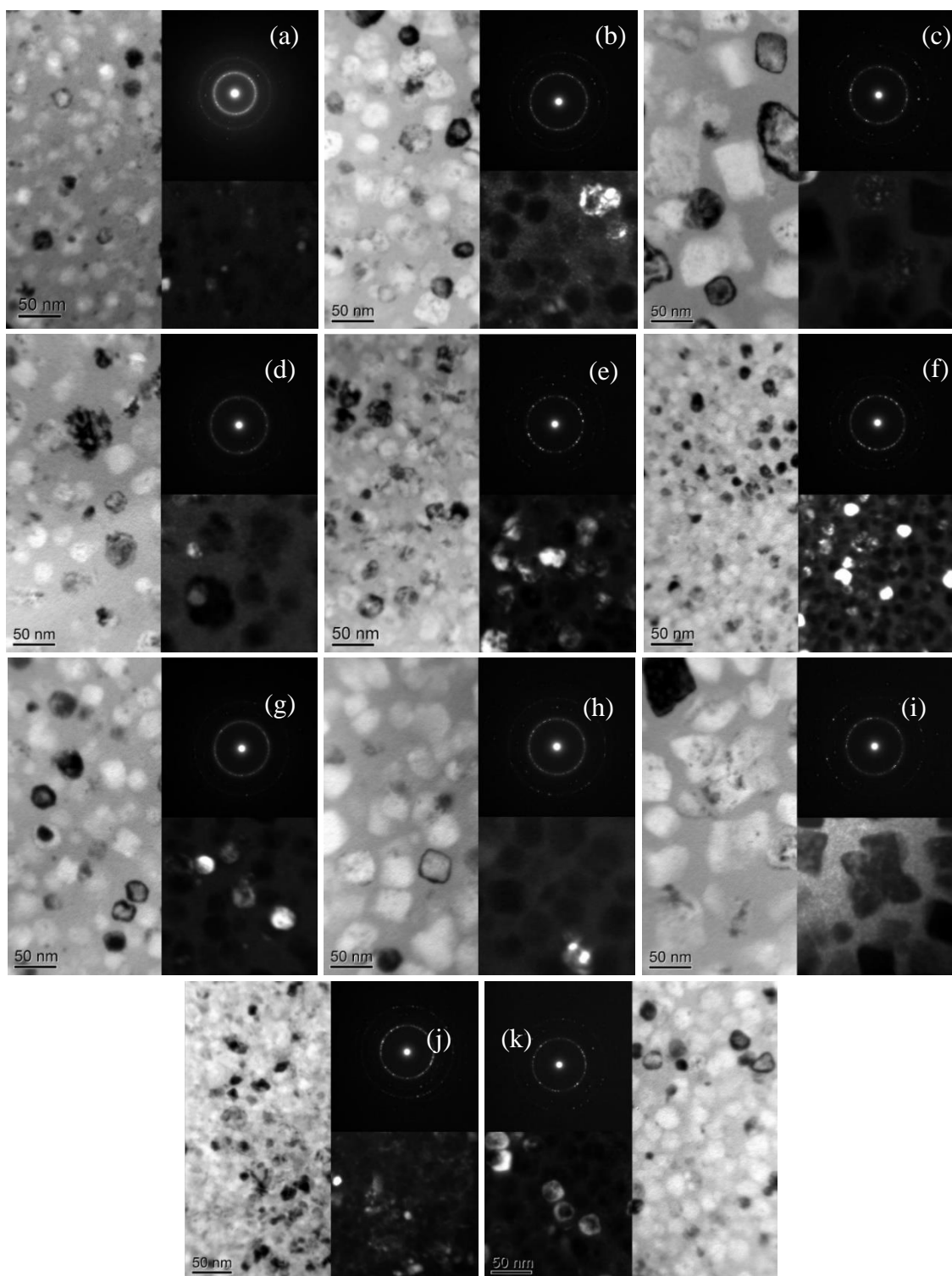


Figure 5.11: Bright field and dark field TEM images and corresponding SAED patterns of (a)  $\text{Fe}_{78}\text{Sn}_7\text{B}_{15}$ , (b)  $\text{Fe}_{81}\text{Sn}_7\text{B}_{12}$ , (c)  $\text{Fe}_{83}\text{Sn}_5\text{B}_{12}$ , (d)  $(\text{Fe}_{78}\text{Sn}_7\text{B}_{15})_{99}\text{Cu}_1$ , (e)  $(\text{Fe}_{81}\text{Sn}_7\text{B}_{12})_{99}\text{Cu}_1$ , (f)  $(\text{Fe}_{83}\text{Sn}_5\text{B}_{12})_{99}\text{Cu}_1$ , (g)  $(\text{Fe}_3\text{Co}_1)_{78}\text{Sn}_7\text{B}_{15}$ , (h)  $(\text{Fe}_3\text{Co}_1)_{81}\text{Sn}_7\text{B}_{12}$ , (i)  $(\text{Fe}_3\text{Co}_1)_{83}\text{Sn}_5\text{B}_{12}$ , (j)  $((\text{Fe}_3\text{Co}_1)_{78}\text{Sn}_7\text{B}_{15})_{99}\text{Cu}_1$ , (k)  $((\text{Fe}_3\text{Co}_1)_{81}\text{Sn}_7\text{B}_{12})_{99}\text{Cu}_1$ . Samples were annealed isothermally at 673 K for 30 min, exception was  $\text{Fe}_{78}\text{Sn}_7\text{B}_{15}$  which was annealed at 648 K for 30 min.

Mean grain size of  $\alpha$ -Fe grains observed from TEM micrographs of selected alloys after thermal treatment that activates first stage of crystallization shown in Figure 5.11 are shown in Figure 5.12.

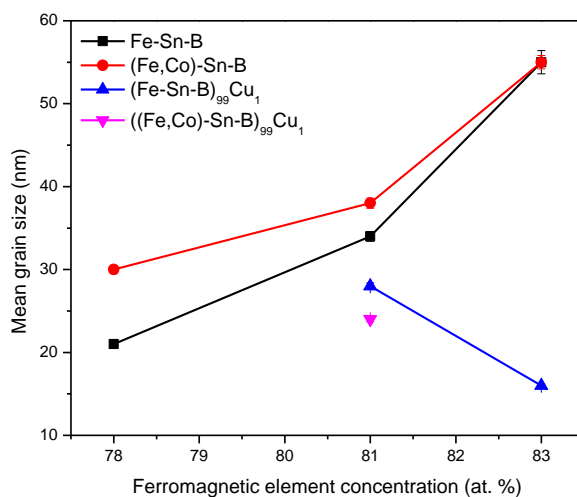


Figure 5.12: Mean grain size vs ferromagnetic element concentration of  $\alpha$ -Fe grains observed from TEM micrographs of selected alloys after thermal treatment that activates first stage of crystallization shown in Figure 5.11.

In the first stage of crystallization approximately 50 % of volume of amorphous matrix crystallizes into  $\alpha$ -Fe phase with bcc structure. Morphology of these systems is similar to the classical nanocrystalline materials mentioned in [26] but without use of early transition metals.

Diffraction patterns of studied alloys after isothermal annealing for 30 min at indicated temperatures that activates second stage of crystallization are shown in Figure 5.12. Bright field and dark field TEM micrographs with SEAD patterns of  $\text{Fe}_{81}\text{Sn}_7\text{B}_{12}$  and  $(\text{Fe}_{81}\text{Sn}_7\text{B}_{12})_{99}\text{Cu}_1$  alloys after isothermal annealing for 30 min at 798 K which was sufficient to activate second stage of crystallization is shown in Figure 5.13. Both  $\text{Fe}_{81}\text{Sn}_7\text{B}_{12}$  and  $(\text{Fe}_{81}\text{Sn}_7\text{B}_{12})_{99}\text{Cu}_1$  alloys shown in Figure 5.13 are fully crystallized. Addition of Cu does not affect morphology in second stage of crystallization.

In the second stage of crystallization the rest of amorphous matrix crystallizes into  $\text{Fe}_2\text{B}$  and  $\text{FeSn}$  phases. Iron oxides  $\text{Fe}_3\text{O}_4$  with cubic structure and  $\text{Fe}_2\text{O}_3$  with rhombohedral structure were also identified. Oxides are most likely present only on samples surface similarly as in [27]. Annealing in air atmosphere may be the reason why iron oxides were present.

Addition of Cu decreases glass forming ability of alloys which resulted in alloys being partially crystallized in as-quenched state. Morphology of studied alloys after thermal treatment that activates first stage of crystallization consists of relatively homogenous distributed  $\alpha$ -Fe nanograins surrounded by amorphous matrix. Increase in amount of Sn changes shape of  $\alpha$ -Fe nanograins from cubical to spherical and also decreases their size. Addition of Co does not affect morphology of alloys while addition of Cu decreases  $\alpha$ -Fe grain size and refines structure. Increase in amount of B from 12 to 15 at. % does not affect morphology of alloys.

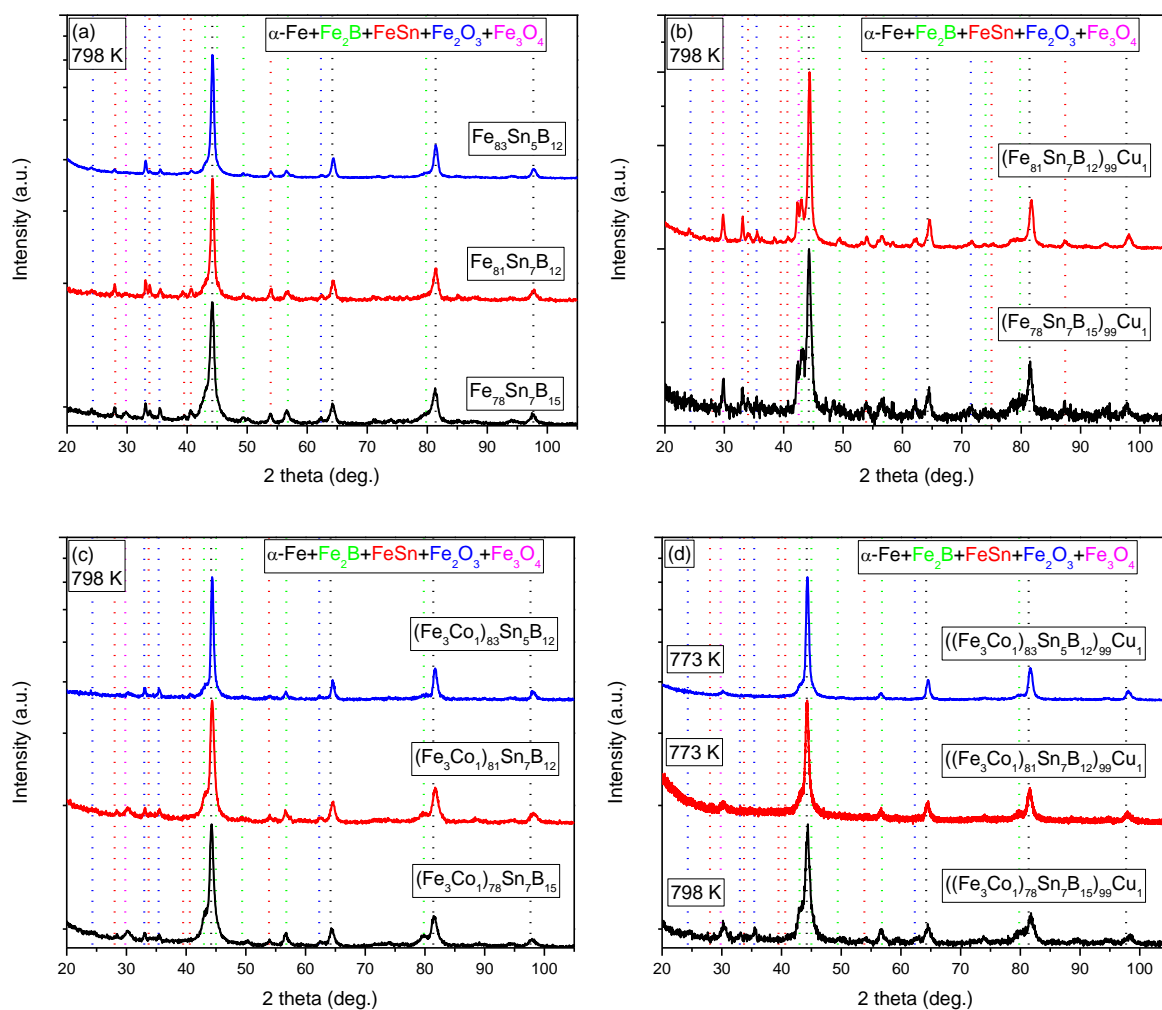


Figure 5.12: XRD patterns of (a) base compositions, (b) alloys with addition of Cu, (c) alloys with addition of Co and (d) alloys with addition of both Cu and Co. After isothermal annealing at indicated temperature for 30 min. Identified phases are listed in the legends at the top of each graph and corresponding peaks are indicated with vertical dotted lines of the same color as phases they correspond to. Individual traces are shifted vertically for clarity.

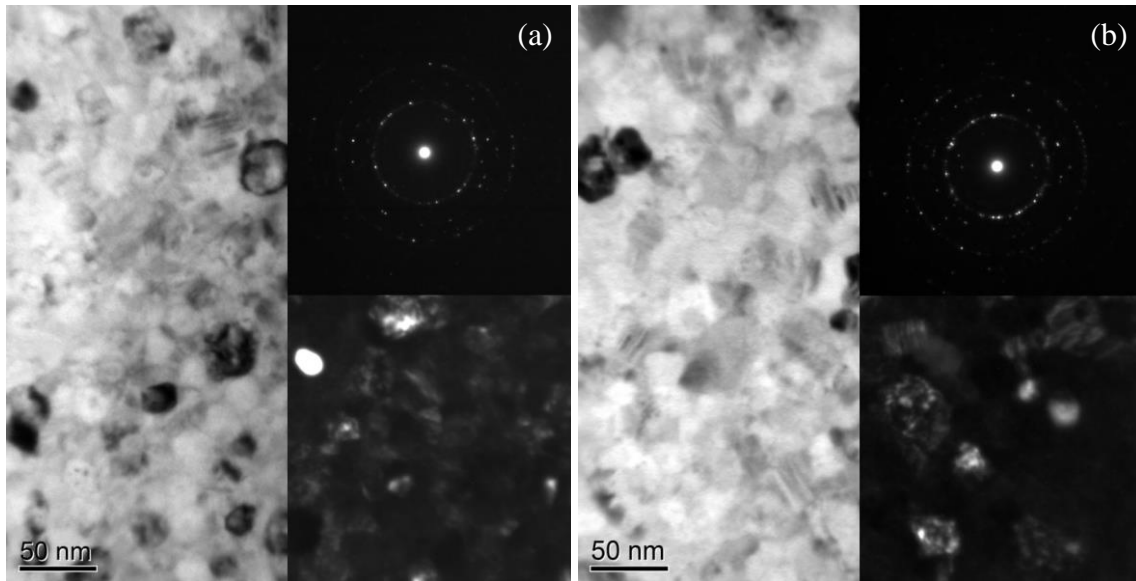


Figure 5.13: Bright field and dark field TEM images and corresponding SAED patterns of fully crystallized (a)  $\text{Fe}_{81}\text{Sn}_7\text{B}_{12}$  and (b)  $(\text{Fe}_{81}\text{Sn}_7\text{B}_{12})_{99}\text{Cu}_1$  alloys. Samples were annealed isothermally at 798 K for 30 min.

Effect of annealing temperature on morphology of  $\text{Fe}_{83}\text{Sn}_5\text{B}_{12}$ ,  $\text{Fe}_{81}\text{Sn}_7\text{B}_{12}$  and  $(\text{Fe}_{81}\text{Sn}_7\text{B}_{12})_{99}\text{Cu}_1$  alloys is shown in Figure 5.14, and calculated mean grain size are shown in Figure 5.15. Results from Figures 5.14 and 5.15 suggested that  $\text{Fe}_{83}\text{Sn}_5\text{B}_{12}$  would exhibit highest mean grains size of  $\alpha$ -Fe phase followed by  $\text{Fe}_{81}\text{Sn}_7\text{B}_{12}$  and  $(\text{Fe}_{81}\text{Sn}_7\text{B}_{12})_{99}\text{Cu}_1$  with lowest mean grain size of  $\alpha$ -Fe phase of the three.

Comparison between mean grain sizes of  $\alpha$ -Fe phase observed from TEM micrographs and results from Rietveld refinement of XRD patterns for selected alloys is shown in Table 5.2. Results from Table 5.2 shows that values of mean grain sizes of  $\alpha$ -Fe phase from TEM match very well with crystal sizes of  $\alpha$ -Fe phase from XRD, which suggests that individual grains visible in TEM micrographs are made of single nanocrystals. Difference between values obtained from TEM and XRD may be results of non-representative part of the sample being chosen in TEM micrographs.

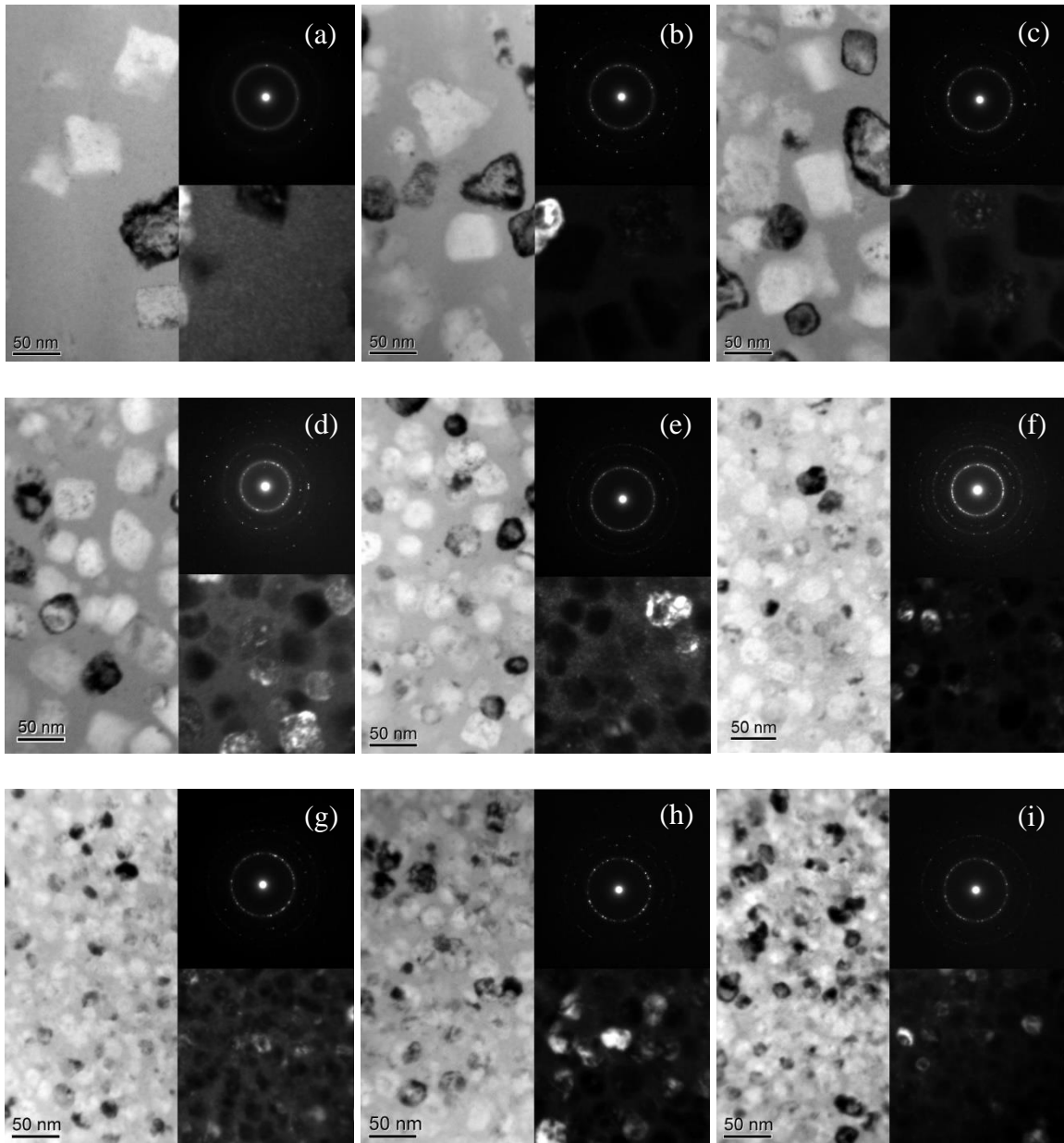


Figure 5.14: Bright field and dark field TEM images and corresponding SAED patterns of selected systems isothermally annealed for 30 min at different temperatures, all sufficient to activate first stage of crystallization but insufficient to activate second stage of crystallization.

$\text{Fe}_{83}\text{Sn}_5\text{B}_{12}$  (a) 623 K, (b) 653 K, (c) 673 K.  $\text{Fe}_{81}\text{Sn}_7\text{B}_{12}$  (d) 648 K, (e) 673 K, (f) 698 K.

$(\text{Fe}_{81}\text{Sn}_7\text{B}_{12})_{99}\text{Cu}_1$  (g) 648 K, (h) 673 K, (i) 698 K.

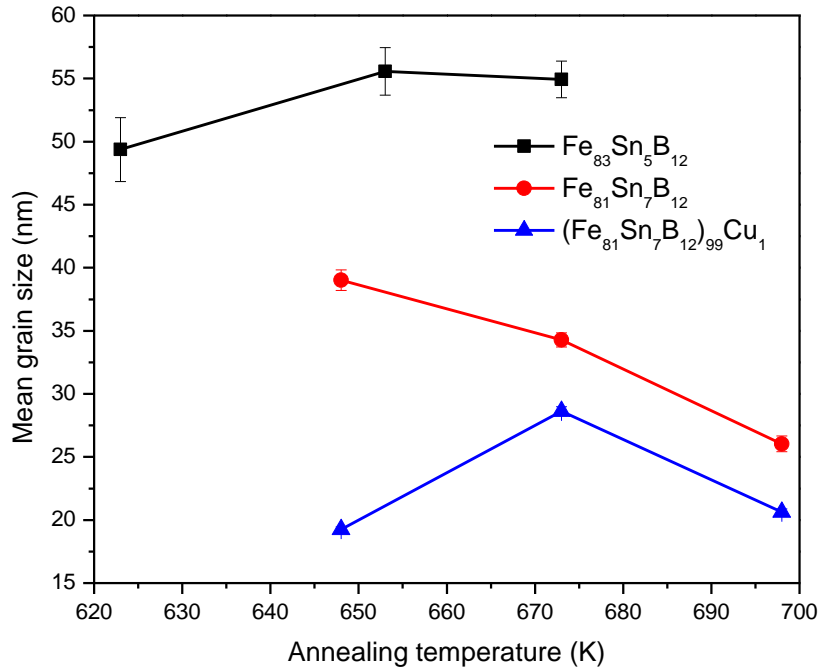


Figure 5.15: Effect of annealing temperature on mean grain size of  $\alpha$ -Fe observed from TEM micrographs shown in Figure 5.14.

Table 5.2: Comparison of mean grain sizes of  $\alpha$ -Fe phase obtained from TEM and crystal sizes of  $\alpha$ -Fe phase obtained from XRD of selected alloys after isothermal annealing at listed temperatures. All Samples were isothermally annealed for 30 min.

Chemical composition	Annealing temperature [K]	Mean grain sizes of $\alpha$ -Fe phase from TEM [nm]	Crystal sizes of $\alpha$ -Fe phase from XRD [nm]
$\text{Fe}_{81}\text{Sn}_7\text{B}_{12}$	648	$39 \pm 0.8$	$42.4 \pm 1.4$
	673	$34 \pm 0.6$	$35.8 \pm 0.8$
	698	$26 \pm 0.6$	$32.3 \pm 0.8$
$(\text{Fe}_{81}\text{Sn}_7\text{B}_{12})_{99}\text{Cu}_1$	648	$19 \pm 0.2$	$15.7 \pm 0.5$
	673	$28 \pm 0.4$	$15.8 \pm 0.5$
	698	$21 \pm 0.3$	$16.7 \pm 0.4$
$(\text{Fe}_3\text{Co}_1)_{78}\text{Sn}_7\text{B}_{15}$	673	$30 \pm 0.5$	$34.4 \pm 1.2$
$(\text{Fe}_3\text{Co}_1)_{81}\text{Sn}_7\text{B}_{12}$	673	$38 \pm 0.6$	$48.6 \pm 1.1$
$(\text{Fe}_{83}\text{Sn}_5\text{B}_{12})_{99}\text{Cu}_1$	673	$16 \pm 0.2$	$17.4 \pm 0.3$
$((\text{Fe}_3\text{Co}_1)_{81}\text{Sn}_7\text{B}_{12})_{99}\text{Cu}_1$	673	$24 \pm 0.3$	$19 \pm 0.5$

Selected alloys were isothermally annealed for 30 min at temperatures from 648 K up to 798 K with 25 K step. Example of diffractograms of samples after thermal treatment as well as of samples in as-quenched state for  $(\text{Fe}_{81}\text{Sn}_7\text{B}_{12})_{99}\text{Cu}_1$  and  $(\text{Fe}_3\text{Co}_1)_{81}\text{Sn}_7\text{B}_{12}$  are shown in Figure 5.16. Detailed analysis of diffractograms of samples that did not reach the second stage of crystallization was done. Crystallized volume fraction and FWHM of the first peak of  $\alpha$ -Fe phase were determined for samples that did not reach the second stage of crystallization and lattice parameter of  $\alpha$ -Fe phase was calculated for all diffractograms. Effect of annealing temperature on lattice parameter of  $\alpha$ -Fe(Sn) phase is shown in Figure 5.17.

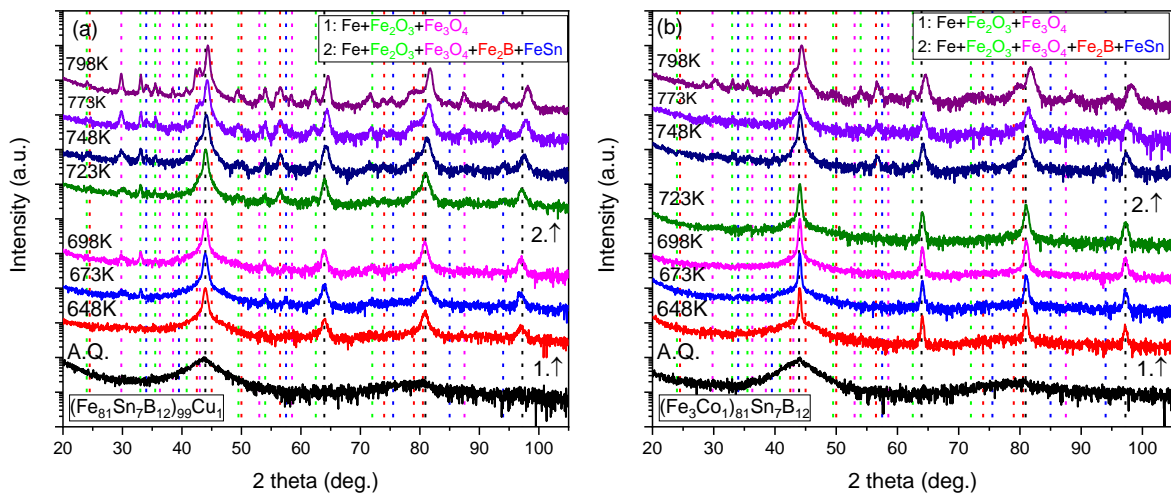


Figure 5.16: XRD patterns of (a)  $(\text{Fe}_{81}\text{Sn}_7\text{B}_{12})_{99}\text{Cu}_1$  and (b)  $(\text{Fe}_3\text{Co}_1)_{81}\text{Sn}_7\text{B}_{12}$  alloys in as-quenched state and after isothermal annealing at indicated temperatures for 30 min. Beginning of the first and the second crystallization stages is indicated by arrows and individual patterns are grouped into two groups that correspond to these two stages of crystallization. Identified phases are listed and corresponding peaks are indicated with vertical dashed lines of the same color as phases they correspond to. Individual traces are shifted vertically for clarity.

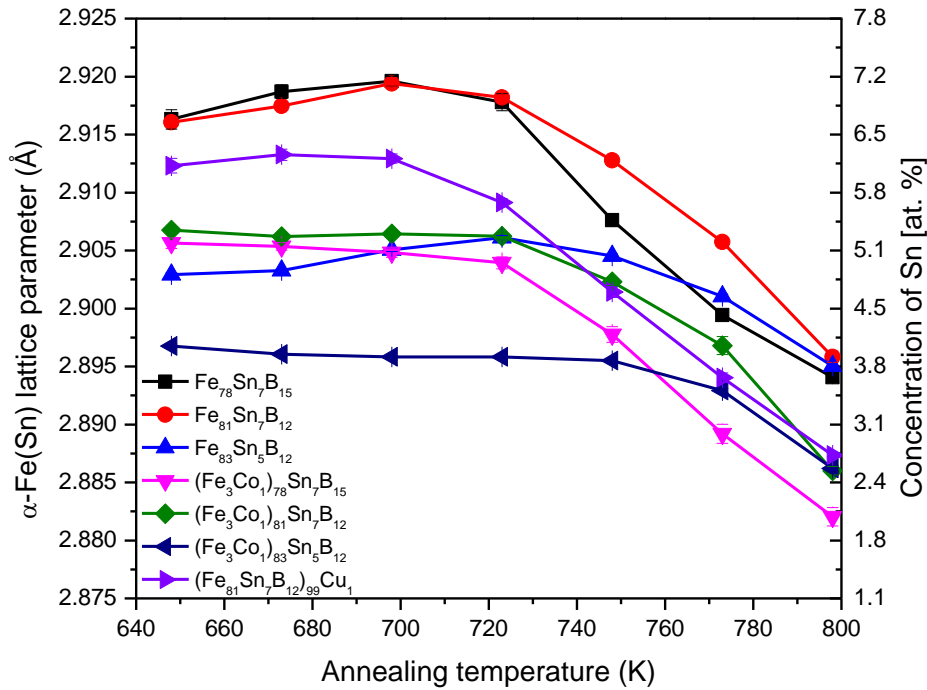


Figure 5.17: Effect of annealing temperature on lattice parameter of  $\alpha$ -Fe(Sn) phase. Concentration of Sn is calculated from Vegard's law.

Concentration of Sn in  $\alpha$ -Fe phase calculated from lattice parameter of  $\alpha$ -Fe phase, increases with temperature of annealing up to a point and then steadily decreases. Maximum concentration of Sn in  $\alpha$ -Fe is close to nominal chemical composition of studied alloys, indicating that Sn is fully dissolved in Fe. Addition of Co visibly decreases and stabilizes lattice parameter. Addition of Cu lowers concentration of Sn in  $\alpha$ -Fe(Sn), and shifts maximum of Sn concentration to lower temperature.

Crystallized volume fraction and FWHM of the first peak of  $\alpha$ -Fe phase as a function of annealing temperature were determined for samples that did not reach the second stage of crystallization and are shown in Figure 5.18. Crystallized volume fraction increases with increase of annealing temperature. Before the second stage of crystallization was activated, 45 % to 55 % volume of studied alloys were crystallized into  $\alpha$ -Fe phase. FWHM of the first peak of  $\alpha$ -Fe phase represents size of  $\alpha$ -Fe crystals. Wider peaks correspond to smaller crystals.  $(\text{Fe}_{81}\text{Sn}_7\text{B}_{12})_{99}\text{Cu}_1$  alloy have wider peaks that correspond to  $\alpha$ -Fe phase.

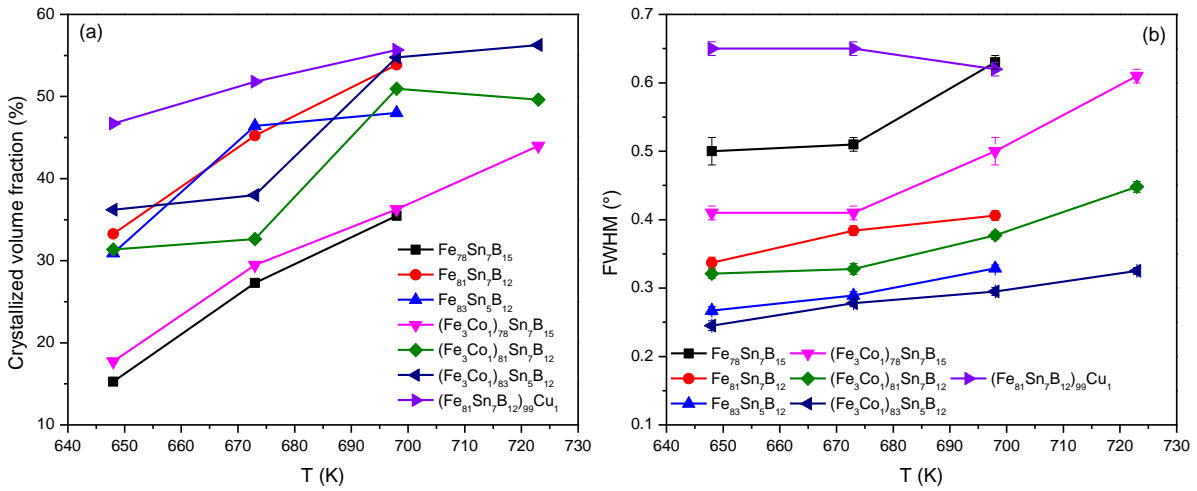


Figure 5.18: Crystallized volume fraction (a) and FWHM of the first peak of  $\alpha$ -Fe phase (b) as a function of annealing temperature of selected alloys. Annealing time 30 min.

Useful comparison of crystal size of different alloys should be done when alloys achieve similar values of crystalline volume fraction. FWHM that corresponds to crystal size and lattice parameter of  $\alpha$ -Fe phase in studied alloys as a function of crystalline volume fraction is shown in Figure 5.19.

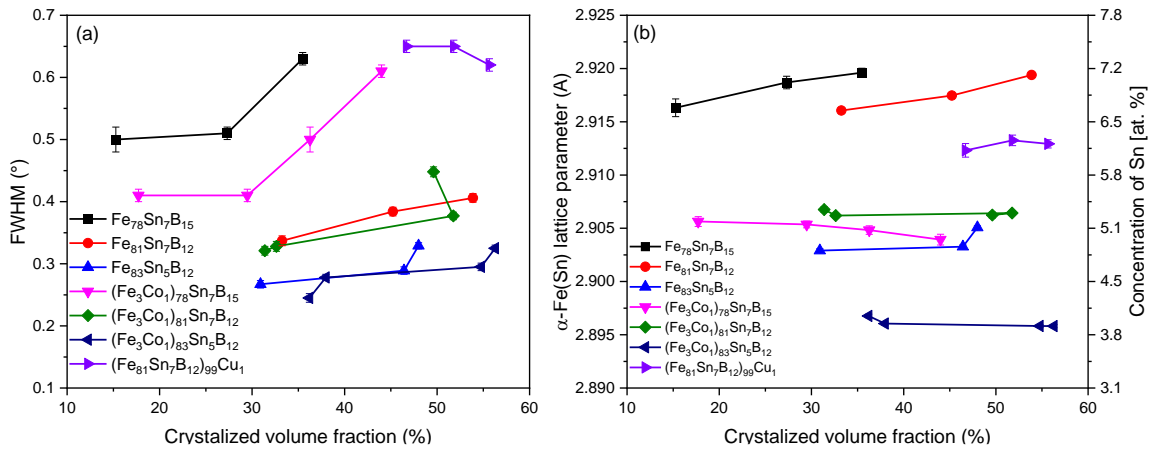


Figure 5.19: FWHM of the first peak of  $\alpha$ -Fe phase (a) and lattice parameter of  $\alpha$ -Fe phase (b) of selected isothermally annealed alloys as functions of crystallized volume fraction.

Crystallization data are taken from experiment analogous to Figure 5.16.

Comparison of FWHM values of the first peak and lattice parameter of  $\alpha$ -Fe phase of studied alloys at similar crystalline volume fraction shows that addition of Co decreases concentration of Sn in  $\alpha$ -Fe phase by 2 at. % in alloys with 7 at. % of Sn and by 1 at. % in alloy with 5 at. % of Sn. Addition of Co slightly increases crystal size of  $\alpha$ -Fe phase, the most noticeably in case

of  $\text{Fe}_{78}\text{Sn}_7\text{B}_{12}$  alloy. Addition of Cu has bigger impact on FWHM values of the first peak of  $\alpha$ -Fe phase which increases by 60 %, indicating decrease in crystal size of  $\alpha$ -Fe phase in  $(\text{Fe}_{81}\text{Sn}_7\text{B}_{12})_{99}\text{Cu}_1$  alloy by 60 % in comparison with  $\text{Fe}_{81}\text{Sn}_7\text{B}_{12}$  alloy at similar value of crystalline volume fraction (50 % - 55 %). Concentration of Sn in  $\alpha$ -Fe phase decreased in  $(\text{Fe}_{81}\text{Sn}_7\text{B}_{12})_{99}\text{Cu}_1$  alloy in comparison with  $\text{Fe}_{81}\text{Sn}_7\text{B}_{12}$  alloy by 0.8 at. %.

Effect of two most common types of thermal treatment, isothermal annealing and annealing in linear heating regime, on microstructure of as-quenched alloy was compared in case of  $\text{Fe}_{81}\text{Sn}_7\text{B}_{12}$  alloy. Diffractograms of samples after thermal treatment as well as of samples in as-quenched state are shown in Figure 5.20. Iron oxides were identified only in diffractograms of isothermally annealed samples. Presence of iron oxides may be a consequence of annealing in air atmosphere and was prevented in case of samples annealed in Ar atmosphere.

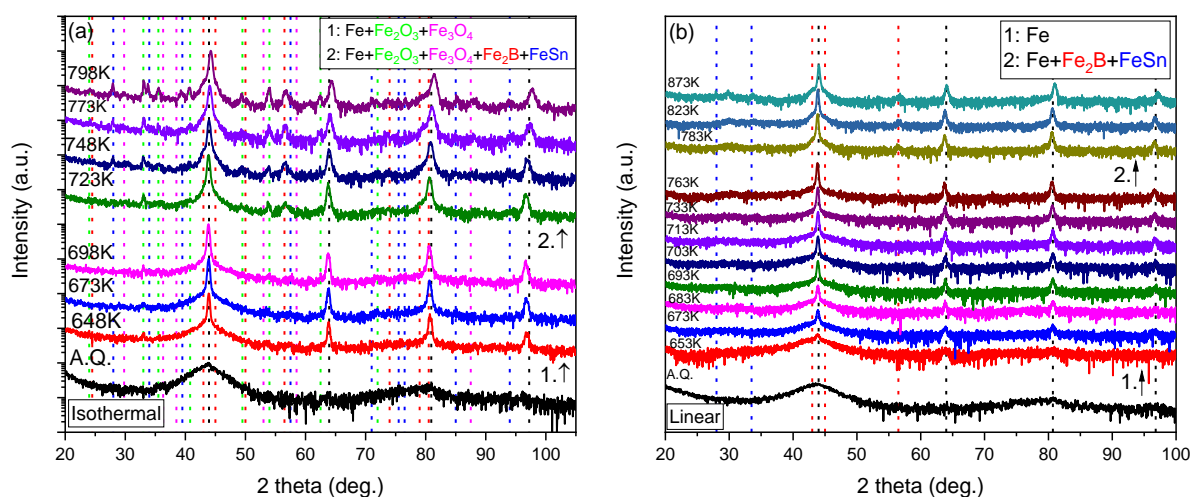


Figure 5.20: XRD patterns of  $\text{Fe}_{81}\text{Sn}_7\text{B}_{12}$  alloy in as-quenched state and after isothermal annealing for 30 min at indicated temperature (a) and after annealing in linear heating regime with heating rate of 20 K/min from room temperature up to indicated temperature (b).

Beginning of first and second crystallization stages is indicated by arrows and individual patterns are grouped into two groups that correspond to these two stages of crystallization. Identified phases are listed and corresponding peaks are indicated with vertical dotted lines of the same color as phases they correspond to. Individual traces are shifted vertically for clarity.

Effect of thermal treatment on lattice parameter of  $\alpha$ -Fe phase, calculated from diffractograms in Figure 5.20 is shown in Figure 5.21. Crystalline volume fraction was calculated from

diffraction patterns of samples that did not achieve second stage of crystallization to show the mentioned effect. Results are shown in Figure 5.22 (a) and it could be seen that samples annealed isothermally for 30 min exhibit about 20 % more crystalline volume fraction than samples annealed in linear heating regime with heating rate of 20 K/min from room temperature up to the same temperature. Because of this effect lattice parameter changes due to linear and isothermal annealing cannot be effectively compared as a function of annealing temperature. For this purpose, the changes of lattice parameter due to linear and isothermal annealing were compared as a function of crystallized volume fraction. Now it is more clear that decrease of lattice parameter of  $\alpha$ -Fe visible in linear annealing results that takes place in the initial part of crystallization process is not visible in isothermal annealing results because they start at higher percentage of crystallinity where results for linear and isothermal annealing are very similar. Taking into consideration results for change in crystal size of  $\alpha$ -Fe phase with increase of annealing temperature calculated from diffraction patterns of samples annealed in linear heating regime shown in Figure 5.22 (b) which shows increase of crystal size of  $\alpha$ -Fe phase in first stage of crystallization and decrease as second stage of crystallization starts, possible explanation could be that after the first stage of crystallization where  $\alpha$ -Fe(Sn) phase increases in volume and temperature approaches  $T_{x2}$ , Sn leaves  $\alpha$ -Fe(Sn) lattice and starts to form FeSn phase partly at the expense of  $\alpha$ -Fe(Sn). Crystal size of  $\alpha$ -Fe phase decreases with increase of annealing temperature in case of samples annealed isothermally.

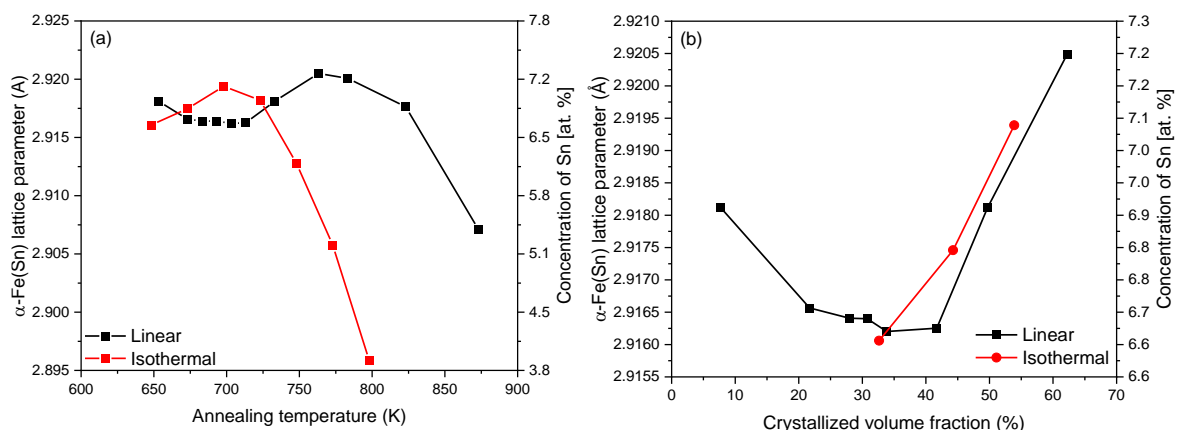


Figure 5.21: Comparison of isothermal annealing and annealing in linear heating regime on evolution of  $\alpha$ -Fe lattice parameter of  $\text{Fe}_{81}\text{Sn}_7\text{B}_{12}$  alloy as a function of annealing temperature (a). Comparison of isothermal annealing and annealing in linear heating regime on evolution of  $\alpha$ -Fe lattice parameter of  $\text{Fe}_{81}\text{Sn}_7\text{B}_{12}$  alloy as a function of crystallized volume fraction (b).

Concentration of Sn is calculated from Vegard's law.

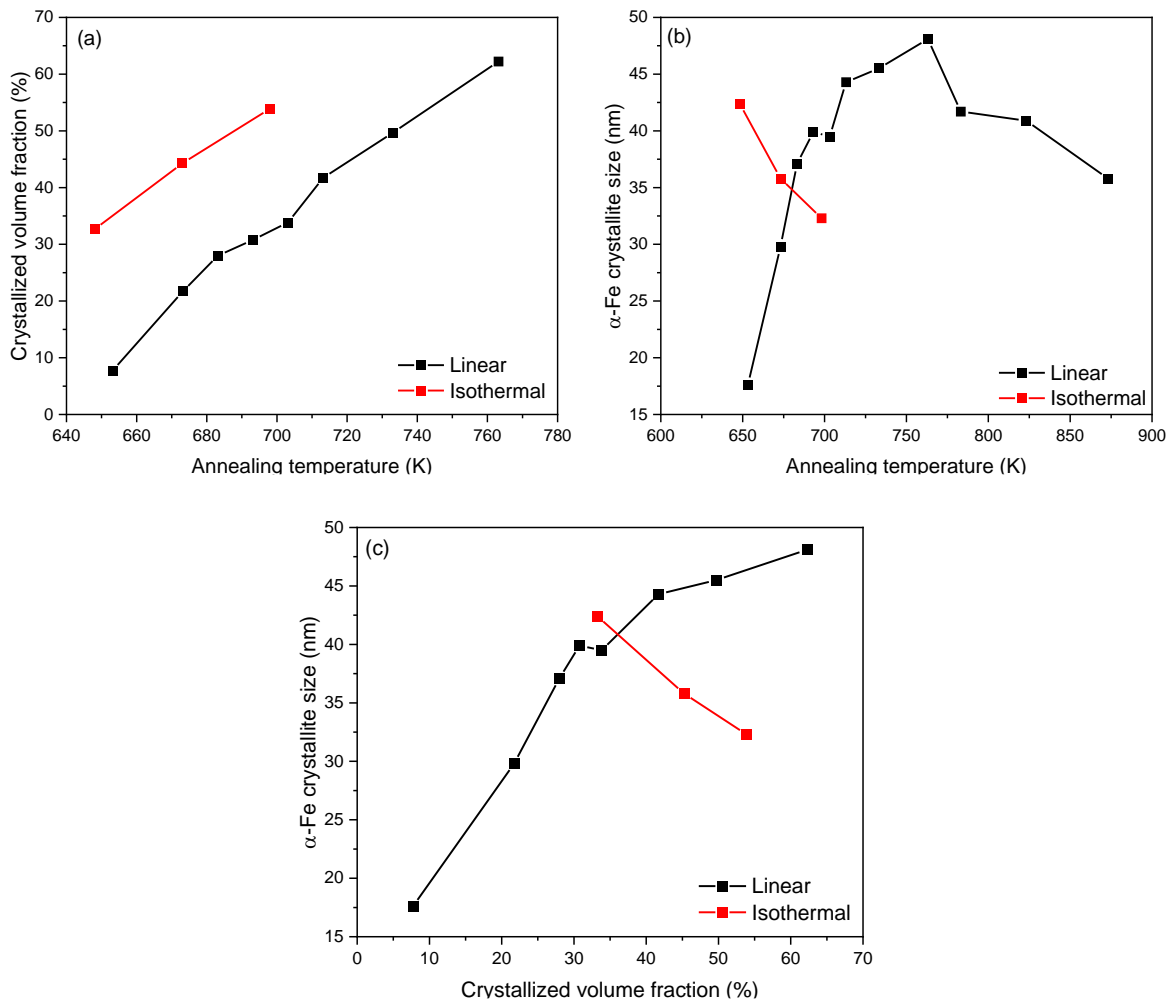


Figure 5.22: Comparison of isothermal annealing and annealing in linear heating regime on development of crystalline phase in Fe<sub>81</sub>Sn<sub>7</sub>B<sub>12</sub> alloy as a function of annealing temperature (a). Calculated size of  $\alpha$ -Fe crystals as a function of annealing temperature (b) and crystallized volume fraction (c).

When compared as a function of crystallized volume fraction in Figure 5.22 (c), crystal size of  $\alpha$ -Fe phase exhibit similar value of 40 nm at 30 % crystallized volume fraction for both samples annealed in linear heating regime and samples annealed isothermally. After which value of crystal size of  $\alpha$ -Fe phase increases with increase in crystallized volume fraction for samples annealed in linear heating regime while in case of samples annealed isothermally crystal size of  $\alpha$ -Fe phase decreases with increase in crystallized volume fraction.

When compared at similar values of crystallized volume fraction both annealing at linear heating regime and isothermal annealing resulted in similar trend in concentration of Sn in  $\alpha$ -Fe phase through crystallization process. Possible explanation could be that after the first stage

of crystallization where  $\alpha$ -Fe phase increases in volume and temperature approaches  $T_{x2}$ , Sn leaves  $\alpha$ -Fe lattice and starts to form FeSn phase.

Local environments of Fe atoms were studied by Mössbauer spectrometry. Base compositions and  $(\text{Fe}_3\text{Co}_1)\text{SnB}$  alloys were annealed in linear heating regime to the end of first step of crystallization. Results were compared with some alloys annealed isothermally in [28]. Mössbauer spectra of  $\text{Fe}_{81}\text{Sn}_7\text{B}_{12}$  alloy with corresponding distributions of hyperfine magnetic fields  $P(B)$  is shown in Figure 5.23. Spectral parameters of fitted sextets in Figure 5.23 are listed in Table 5.3.

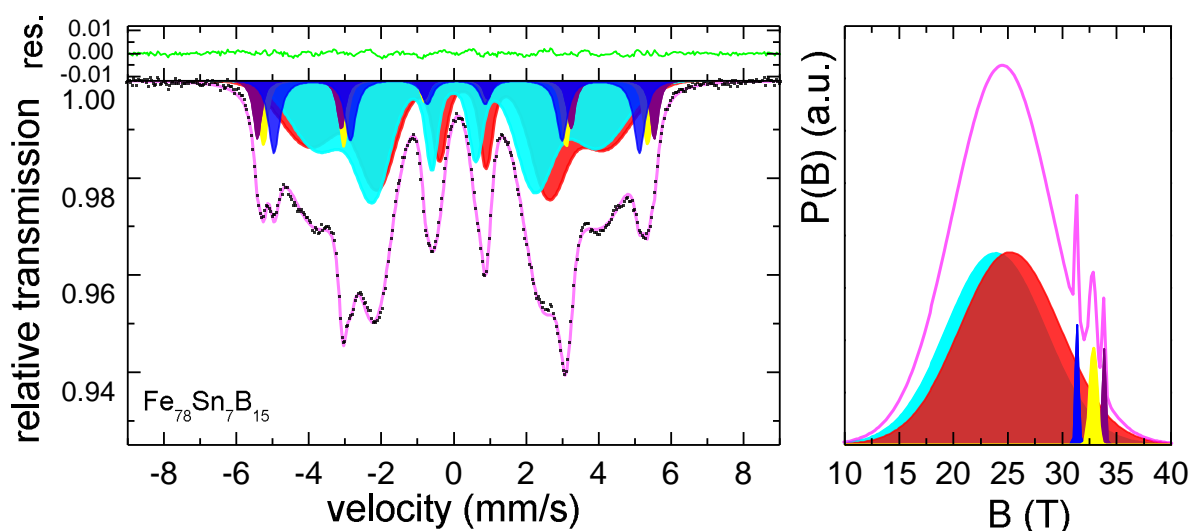


Figure 5.23: Mössbauer spectra of  $\text{Fe}_{78}\text{Sn}_7\text{B}_{15}$  alloy annealed in linear heating regime with heating rate of 20 K/min from room temperature up to temperature just before start of the second stage of crystallization with corresponding distributions of hyperfine magnetic fields  $P(B)$ .

Table 5.3: Spectral parameters of fitted sextets in Figure 4.36.

Component	$A_{\text{rel}}$	$\delta$ [mm/s]	$R_{21}$	B [T]
A 1	0.38	0.07	1	23.88
A 2	0.38	0.18	1	25.26
C 1	0.07	0.04	0.93	32.94
C 2	0.06	0.06	0.93	34.04
C 3	0.11	0.08	0.93	31.35

Results for crystalline volume fractions were in agreement with results from XRD measurements. Net magnetic moment of all samples was tilted towards ribbon plane except  $\text{Fe}_{83}\text{Sn}_7\text{B}_{12}$  which exhibit value of  $R_{21}$  parameter that corresponds to random orientation. Average hyperfine magnetic field of amorphous phase was not influenced by addition of Co. Isothermally annealed samples exhibit higher values of  $B_{\text{am}}$  25 T compared with 24 T for samples annealed in linear heating regime. Difference in  $B_{\text{am}}$  value may be result of samples annealed isothermally exhibit lower crystalline volume fractions. Crystallization of  $\alpha$ -Fe phase decrease concentration of Fe atoms in amorphous matrix therefore decreasing value of  $B_{\text{am}}$ .

Average  $B_{\text{cr}}$  exhibit similar values in Fe-Sn-B alloys annealed both linearly and isothermally around 32.5 T. Addition of Co increased value of hyperfine magnetic field of crystalline phase. Average hyperfine magnetic field of samples increased with increase of Fe content from 26.5 T in case of sample with 78 at. % of Fe to 28 T in case of sample with 83 at. % of Fe. Samples annealed linearly exhibit lower average hyperfine magnetic field due to lower crystalline volume fraction.

### 5.3 Magnetic properties

Magnetic thermogravimetry measurements were done to determine  $T_c$  of studied systems. M-TGA curves of selected systems are shown in Figure 5.24. Shape of M-TGA curves presented in this work consist of five intervals. In the first weight starts to decrease, this indicates that temperature is close to  $T_c$  of amorphous matrix. Weight does not decrease to zero because  $T_{x1}$  is lower than  $T_c$  of amorphous matrix and measured curve is superposition of decrease of weight of amorphous matrix and increase of weight of magnetic phase that crystallizes in the first stage of crystallization. Result is the second interval where weight increase before it decreases again in the third interval because temperature approaches  $T_c$  of ferromagnetic phase, but again weight does not fall to zero because  $T_{x2}$  is lower than  $T_c$  of ferromagnetic phase. At this point intervals four and five are quite self explanatory. Increase of weight is consequence of growth of ferromagnetic phases that crystallize in the second stage of crystallization and decrease in weight is consequence of their  $T_c$ . M-TGA measurements show that addition of Co increases  $T_c$  of as-quenched samples and addition of Cu does not have effect on  $T_c$ . Increase in amount of B both and Sn resulted in increase in  $T_c$ .

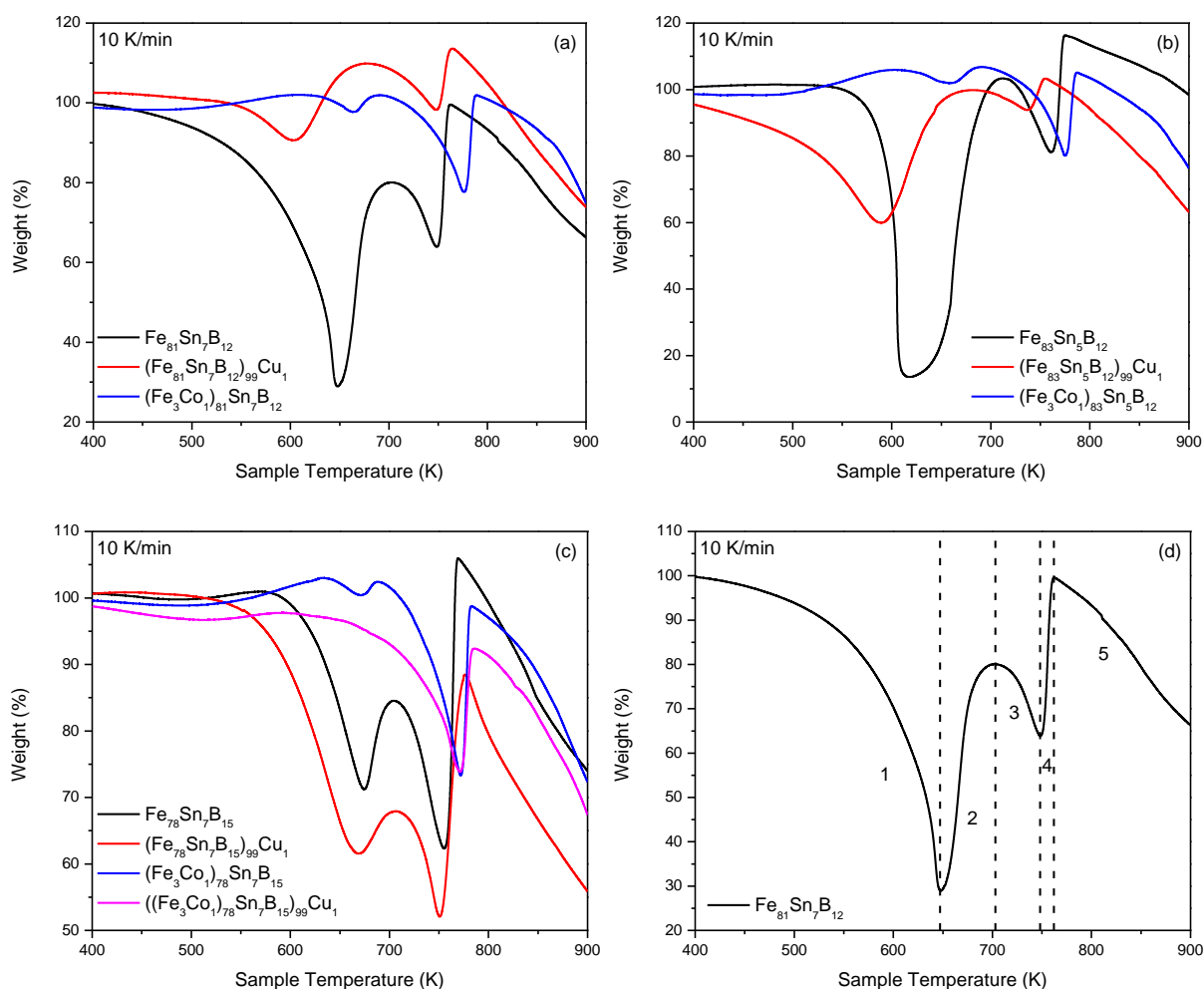


Figure 5.24: M-TGA curves of selected systems with (a) system with 81 at. % of ferromagnetic elements, (b) 83 at. % of ferromagnetic elements, (c) 78 at. % of ferromagnetic elements and (d) M-TGA curve of  $\text{Fe}_{81}\text{Sn}_7\text{B}_{12}$  alloy characteristic intervals.

Magnetic properties of an alloy such as saturation magnetization  $M_s$  and coercive field  $H_c$  are important, among others, for industrial applications. Magnetic hysteresis loops of studied alloys in as-quenched state are shown in Figure 5.25. Effect of thermal treatment on hysteresis loops of selected alloys is shown in Figure 5.26.

Value of saturation magnetization of as-quenched alloys increased with increase in ferromagnetic element. Addition of Cu, Co or both does not show clear trend in relationship with  $M_s$ . Coercive field of as-quenched alloys exhibited similar values in case of alloys with base composition and with addition of Co. Values of  $H_c$  increased for samples with addition of Cu which could be result of these samples exhibiting presence of  $\alpha$ -Fe phase in as-quenched state.

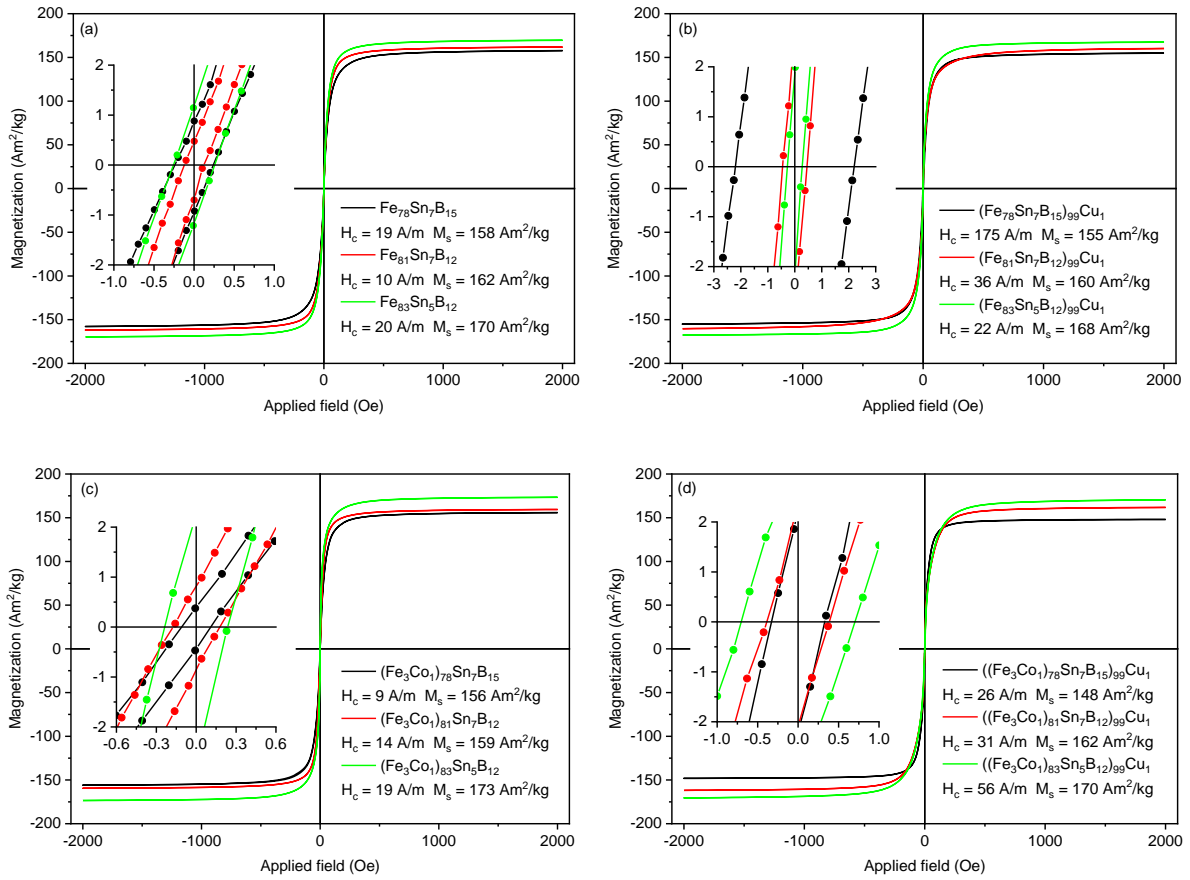


Figure 5.25: Magnetic hysteresis loops of studied alloys in as-quenched state. Base compositions (a). Alloys with addition of Cu (b). Alloys with addition of Co (c). Alloys with addition of both Cu and Co (d).

Thermal treatment of selected alloys, which activate first stage of crystallization increased saturation magnetization. Increase in annealing temperature of alloys annealed isothermally increased saturation magnetization which was not the case for sample annealed in linear heating regime where increase of annealing temperature does not show clear effect on saturation magnetization. Thermal treatment that activated second stage of crystallization decreased value of saturation magnetization, coercive field was drastically increased, and alloys lost good soft magnetic properties. Value of coercive field slightly changed after thermal treatment with no clear trend with temperature of annealing. Lowest value of coercive field by alloys in as-quenched state was achieved by  $(\text{Fe}_3\text{Co}_1)_{78}\text{Sn}_7\text{B}_{15}$  and  $\text{Fe}_{81}\text{Sn}_7\text{B}_{12}$  exhibiting 9 A/m and 10 A/m respectively. Best combination of high saturation magnetization and low coercive field was achieved by  $(\text{Fe}_{83}\text{Sn}_5\text{B}_{12})_{99}\text{Cu}_1$  alloy after annealing in linear heating regime from room temperature up to 603 K with  $M_s = 181 \text{ Am}^2/\text{kg}$  and  $H_c = 17 \text{ A/m}$ .

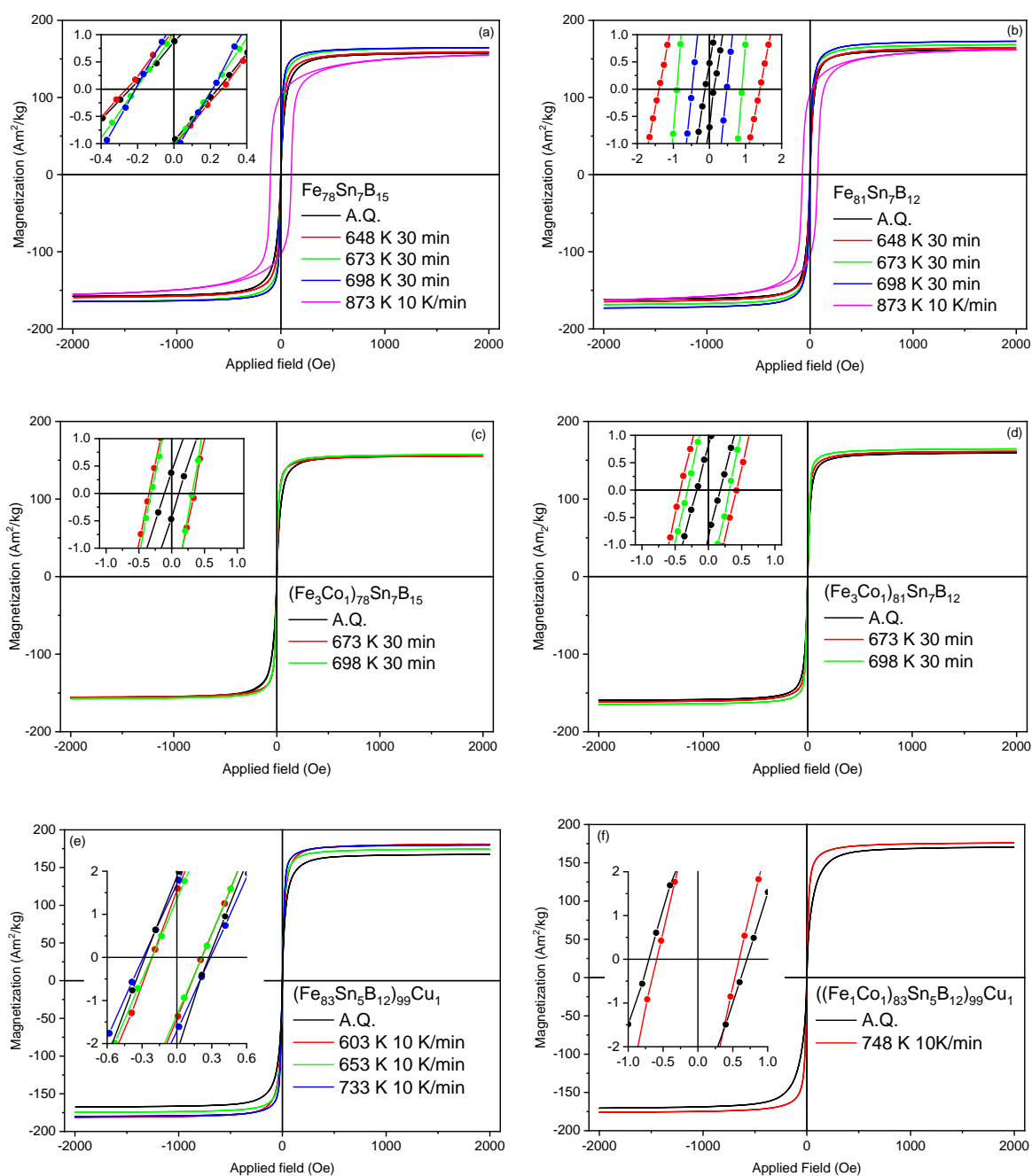


Figure 5.26: Comparison of magnetic hysteresis loops of selected alloys in as-quenched state and after selected types of thermal treatments indicated. Base compositions  $\text{Fe}_{78}\text{Sn}_7\text{B}_{15}$  and  $\text{Fe}_{81}\text{Sn}_7\text{B}_{12}$  are shown in (a) and (b). Addition of Co to base compositions  $\text{Fe}_{78}\text{Sn}_7\text{B}_{15}$  and  $\text{Fe}_{81}\text{Sn}_7\text{B}_{12}$  are shown in (c) and (d). Addition of Co and of both Cu and Co to  $\text{Fe}_{83}\text{Sn}_5\text{B}_{12}$  are shown in (e) and (f).

## 6 Conclusion

Fe-Sn-B based alloys with selected chemical composition were prepared by planar flow casting technology. Effects of variation in iron, boron and tin concentration as well as addition of Co and Cu on various physical properties of studied alloys were investigated. As-quenched alloys exhibit amorphous structure except alloys with addition of Cu which were partially crystallized. Methods selected for thermal analysis, structural analysis and observation and magnetic properties include: DSC, XRD, TEM, TGA, resistometry, Mössbauer spectrometry and VSM.

Crystallization processes were observed in linear heating regime by DSC and resistometry and in isothermal regime by resistometry. Onset temperature of crystallization, temperature of the maximum rate of crystallization and activation energy were determined for both stages of crystallization for all studied alloys. Crystallization kinetics was studied under the framework of the Johnson-Mehl-Avrami-Kolmogorov model. Local activation energies and local Avrami exponents were calculated and used for simulation. Experimental and simulated results were in good agreement.

Products of crystallization were identified by XRD and observed by TEM. Morphology of studied alloys after first stage of crystallization is comparable with commercial alloys such as NANOMET and consists of  $\alpha$ -Fe nanograins embedded in amorphous matrix. In second stage of crystallization the rest of amorphous matrix crystallizes into  $\text{Fe}_2\text{B}$  and  $\text{FeSn}$  phases. Effect of chemical composition of alloy, annealing temperature and annealing regime (linear vs isothermal) on grain size, crystalline volume fraction and lattice parameter of  $\alpha$ -Fe phase was thoroughly investigated.

Mössbauer spectrometry was used as complementary method for structural analysis to XRD and TEM. Hyperfine interaction in selected Fe-Sn-B based alloys was already known for isothermally annealed alloys. After thorough comparison of isothermal and linear annealing on crystal lattice and grains of  $\alpha$ -Fe phase, additional contribution of this work was comparison of isothermal and linear annealing on local environments of individual Fe atoms.

Magnetic properties are important for industrial applications of materials. Studied alloys are magnetically soft in as-quenched state as well as after first stage of crystallization. Second stage of crystallization increases coercive field of studied alloys and they are no longer magnetically

soft. Effect of chemical composition and annealing on saturation magnetization, coercive field and Curie temperature were studied.

Results obtained in this work shows that Fe-Sn-B based alloys can exhibit comparable morphology to classical nanocrystalline materials. These alloys can be potential alternative to NANOMET-like alloys and because of very good soft magnetic properties could be useful for industrial applications.

## 7 Záver

Zliatiny na baze Fe-Sn-B s vybraným chemickým zložením boli pripravené metódou rovinného liatia. Vplyv obsahu železa boru a cínu ale aj pridania Co a Cu na vybrane fyzikálne vlastnosti študovaných zliatin bol preskúmaný. Po výrobe, zliatiny vykazujú amorfnú štruktúru, výnimkou sú zliatiny obsahujúce Cu ktoré boli čiastočne kryštalické. Vybrane metódy termálnej, štruktúrnej a magnetickej analýzy zahŕňajú: DSC, XRD, TEM, TGA, rezistometriu, Mössbauerovu spektrometriu a VSM.

Kryštalizačný proces bol sledovaný v režime lineárneho ohrevu použitím DSC a rezistometrie a tiež v izotermickom režime použitím rezistometrie. Teploty nástupu kryštalizácie, teplota v maxime rýchlosti kryštalizácie a aktivačné energie boli určené pre oba stupne kryštalizácie pre všetky študované zliatiny. Kinetika kryštalizácie bola študovaná v rámci Johnson-Mehl-Avrami-Kolmogorov modelu. Hodnoty lokálnej aktivačnej energie a lokálneho Avramiho exponent boli vypočítané a overené pomocou simulácie.

Produkty kryštalizácie boli identifikované použitím XRD a pozorované pomocou TEM. Morfológia študovaných zliatin po prvom stupni kryštalizácie je porovnateľná s komerčne vyrábanými zliatinami ako NANOMET a pozostáva z nanokryštálov alfa železa vložených v amorfnej matrici. V druhom stupni kryštalizácie, zvyšok amorfnej matrice kryštalizuje do Fe<sub>2</sub>B a FeSn fáz. Vplyv chemického zloženia, teploty žihania a režimu žihania (izotermalny alebo lineárny) na veľkosť zŕn, obsah kryštalickej fázy a mriežkového parametra  $\alpha$ -Fe fázy bol dôkladne preskúmaný.

Mössbauerova spektrometria bola použitá ako komplementárna metóda štruktúrnej analýzy k XRD a TEM výsledkom. Hyperjemné interakcie vo vybraných zliatinách na baze Fe-Sn-B boli už známe pre izotermicky žíhané zliatiny. Po dôkladnom porovnaní izotermalne a lineárne žíhaných vzoriek z pohľadu mriežkového parametra a veľkosti zŕn  $\alpha$ -Fe fázy. Dodatočný prínos tejto práce bolo aj porovnanie vplyvu izotermalneho a lineárneho žihania na lokálne prostredie rezonančných Fe atómov.

Magnetické vlastnosti sú dôležité z pohľadu priemyselných aplikácií materiálov. Študované zliatiny boli magneticky mäkké po výrobe a tiež po prvom stupni kryštalizácie. Druhý stupeň kryštalizácie zväčšil hodnotu koercitívneho poľa študovaných zliatin a už neboli magneticky

mäkké. Vplyv chemického zloženia a žihania na magnetické vlastnosti študovaných systémov bol preskúmaný.

Získané výsledky ukazujú že zliatiny na baze Fe-Sn-B môžu vykazovať podobnú mikroštruktúru ako klasické nanokryštalické materiáli. Tieto zliatiny môžu predstavovať potenciálnu alternatívu zliatinám podobným ako NANOMET kvôli svojim magnetickým vlastnostiam vhodným na priemyselné použitie.

## 8 References

- [1] R. A. Dunlap, "Sn and Fe hyperfine field distributions in the amorphous ferromagnet Fe<sub>80-x</sub>Sn<sub>x</sub>B<sub>20</sub>," *Solid State Communications*, vol. 43, no. 1, pp. 57-60, 1982.
- [2] L. Battezzati, C. Antonione and G. Riontino, "Kinetics of formation and thermal stability of Fe-X-B metallic glasses," *Journal of Non-Crystalline Solids*, vol. 89, pp. 114-130, 1987.
- [3] B. Arcondo, A. Lorenzo, F. Audebert and H. Sirkin, "Glass forming tendency in the FeBSn system," *Hyperfine Interactions*, vol. 83, pp. 281-288, 1994.
- [4] E. Illekova, I. Matko and P. Svec, "The crystallization behavior of amorphous Fe–Sn–B ribbons," *Journal of Alloys and Compounds*, vol. 509, no. Supplement 1, pp. S46-S51, 2011.
- [5] I. Matko, E. Illekova and P. Svec, "Microstructural study of the crystallization of amorphous Fe–Sn–B ribbons," *Journal of Alloys and Compounds*, vol. 615, no. Supplement 1, pp. S462-S466, 2014.
- [6] M. B. Miglierini and V. S. Rusakov, "<sup>57</sup>Fe and <sup>119</sup>Sn Mössbauer Effect Study of Fe–Sn–B Amorphous Alloys," *AIP Conference Proceedings*, vol. 1258, no. 1, p. 29, 2010.
- [7] X. Li, L. Jinbao and Q. Changrong, "Preparation and properties of FeBPSn soft magnetic amorphous alloys with Fe contents higher than 83%," *Journal of Non-Crystalline Solids*, vol. 469, pp. 27-30, 2017.
- [8] L. Shi, K. Wang and K. Yao, "Maintaining high saturation magnetic flux density and reducing coercivity of Fe-based amorphous alloys by addition of Sn," *Journal of Non-Crystalline Solids*, vol. 528, p. 119710, 2020.
- [9] P. Švec, I. Janotová, J. Zigo, I. Matko, D. Janičkovič, J. Marcin, I. Škorvánek and P. Švec Sr., "Selected Trends in New Rapidly Quenched Soft Magnetic Materials," in *Recent Advances in Systems, Control and Information Technology*, 2016.
- [10] L. Wang, L. Zhao, B. Zhang, W. Hu, X. Shu, X. Sheng and Z. Fang, "Crystallization study of electroless Fe–Sn–B amorphous alloy deposits," *Journal of Alloys and Compounds*, vol. 287, no. 1-2, pp. 234-238, 1999.
- [11] H. Okamoto, *Phase Diagrams of Binary Iron Alloys*, ASM International, Materials Park, 1993.
- [12] F. Wang, A. Inoue and Y. Han, "Excellent soft magnetic Fe-Co-B-based amorphous alloys with extremely high saturation magnetization above 1.85 T and low coercivity below 3 A/m," *Journal of Alloys and Compounds*, vol. 711, pp. 132-142, 2017.

- [13] F. Wang, A. Inoue and Y. Han, "Soft magnetic Fe-Co-based amorphous alloys with extremely high saturation magnetization exceeding 1.9 T and low coercivity of 2 A/m," *Journal of Alloys and Compounds*, vol. 723, pp. 376-384, 2017.
- [14] M. Kuhnt, X. Xu and M. Amalraj, "The effect of Co addition on magnetic and structural properties of nanocrystalline (Fe,Co)-Si-B-P-Cu alloys," *Journal of Alloys and Compounds*, vol. 766, pp. 686-693, 2018.
- [15] P. Gabbott, *Principles and Applications of Thermal Analysis*, Oxford: Blackwell Publishing, 2008.
- [16] M. Avrami, "Kinetics of Phase Change. I General Theory," *The Journal of Chemical Physics*, vol. 7, p. 1103, 1939.
- [17] M. Avrami, "Kinetics of Phase Change. II Transformation-Time Relations for Random Distribution of Nuclei," *The Journal of Chemical Physics*, vol. 8, p. 212, 1940.
- [18] M. Avrami, "Granulation, Phase Change, and Microstructure Kinetics of Phase Change. III," *The Journal of Chemical Physics*, vol. 9, p. 177, 1941.
- [19] H. E. Kissinger, "Reaction Kinetics in Differential Thermal Analysis," *Analytical Chemistry*, vol. 29, no. 11, pp. 1702-1706, 1957.
- [20] T. Akahira and T. T. Sunuse, "Joint Convention of Four Electrical Institutes," *Research Report, Chiba Institute of Technology*, vol. 16, pp. 22-31, 1971.
- [21] J. S. Blázquez, C. F. Conde and A. Conde, "Non-isothermal approach to isokinetic crystallization processes: Application to the nanocrystallization of HITPERM alloys," *Acta Materialia*, vol. 53, no. 8, pp. 2305-2311, 2005.
- [22] L. H. Kong, Y. L. Gao, T. T. Song, G. Wang and Q. J. Zhai, "Non-isothermal crystallization kinetics of FeZrB amorphous alloy," *Thermochimica Acta*, vol. 522, no. 1-2, pp. 166-172, 2011.
- [23] S. Ranganathan and M. Von Heimendahl, "The three activation energies with isothermal transformations: applications to metallic glasses," *Journal of Materials Science*, vol. 16, pp. 2401-2404, 1981.
- [24] M. J. Duarte, A. Kostka, D. Crespo, J. A. Jimenez, A. C. Dippel, F. U. Renner and G. Dehm, "Kinetics and crystallization path of a Fe-based metallic glass alloy," *Acta Materialia*, vol. 127, pp. 341-350, 2017.
- [25] T. Paul, A. Loganathan, A. Agarwal and S. P. Harimkar, "Kinetics of isochronal crystallization in a Fe-based amorphous alloy," *Journal of Alloys and Compounds*, vol. 753, pp. 679-687, 2018.

- [26] M. E. McHenry, M. A. Willard and D. E. Laughlin, "Amorphous and nanocrystalline materials for applications as soft magnets," *Progress in Materials Science*, vol. 44, no. 4, pp. 291-433, 1999.
- [27] B. Butvinova, P. Butvin, I. Matko and M. Kedlecikova, "Impact of surfaces on the magnetic properties of Fe-based nanocrystalline ribbons," *Applied Surface Science*, vol. 538, 2021.
- [28] D. G. Grey, *Microstructure of Fe-Sn-B-type metallic glasses with addition of Co*, Slovak University of Technology in Bratislava Faculty of Electrical Engineering and Information Technology, Diploma thesis, 2021.
- [29] R. A. Dunlap, "Sn AND Fe HYPERFINE FIELD DISTRIBUTIONS IN THE AMORPHOUS FERROMAGNET Fe<sub>80-x</sub>Sn<sub>x</sub>B<sub>20</sub>," *Solid State Communications*, vol. 43, no. 1, pp. 57-60, 1982.
- [30] L. Battezzati, C. Antonione and G. Riontino, "KINETICS OF FORMATION AND THERMAL STABILITY OF Fe-X-B METALLIC GLASSES," *Journal of Non-Crystalline Solids*, vol. 89, pp. 114-130, 1987.
- [31] D. Janovszky, M. Sveda, A. Sycheva, F. Kristaly, F. Zámberszky, T. Koziel, P. Bala, G. Czel and G. Kaptay, "Amorphous alloys and differential scanning calorimetry (DSC)," *Journal of Thermal Analysis and Calorimetry*, vol. 147, p. 7141–7157, 2022.
- [32] W. Zhang, P. Tao, Y. Chen, J. Si, Z. Huang, K. Zhu and Y. Yang, "Study on isothermal crystallization kinetics of Zr<sub>55.7</sub>Cu<sub>22.4</sub>Ni<sub>7.2</sub>Al<sub>14.7</sub> bulk amorphous alloy," *Scientific Reports*, vol. 12, p. 5060, 2022.
- [33] T. Xu, X. Li, G. Li, L. Zhuo, E. Yin and Z. Jian, "Tuning crystallization kinetics by high-content solvent element substitution between Cr<sub>45</sub>Fe<sub>11</sub>Co<sub>7</sub>Mo<sub>14</sub>C<sub>15</sub>B<sub>6</sub>Y<sub>2</sub> and Fe<sub>41</sub>Cr<sub>15</sub>Co<sub>7</sub>Mo<sub>14</sub>C<sub>15</sub>B<sub>6</sub>Y<sub>2</sub> metallic glasses," *Thermochimica Acta*, vol. 703, p. 179013, 2021.
- [34] T. Xu, Z. Jian, L. Zhuo, F. Chang, M. Zhu, Y. Liu and Z. Jie, "Nonisothermal crystallization kinetics of Cr-rich metallic glass Cr<sub>29.4</sub>Fe<sub>29.4</sub>Mo<sub>14.7</sub>C<sub>14.7</sub>B<sub>9.8</sub>Y<sub>2</sub> with desirable properties," *International Journal of Chemical Kinetics*, vol. 53, no. 7, pp. 815-824, 2021.
- [35] G. Herzer, "Modern soft magnets: Amorphous and nanocrystalline materials," *Acta Materialia*, vol. 61, no. 3, pp. 718-734, 2013.

## 9 List of publications

### Articles

1. **A. Fos**, P. Švec, I. Janotová, D. Janičkovič, B. Butvinová, M. Búran, A. Kyritsi, N. Konstantinidis, P. Novák. Effect of Cu and Co addition on non-isothermal crystallization kinetics of rapidly quenched Fe-Sn-B based alloys. *Journal of Non-Crystalline Solids*, 593. s. 2022.
2. B. Butvinová, P. Švec, I. Janotová, **A. Fos**, I. Maťko, D. Janičkovič. Magnetic and structural properties of  $(\text{Fe-Co})_{83}(\text{Sn-P})_5\text{B}_{12}$  alloys with high saturation. *Journal of Magnetism and Magnetic Materials*, 535. s. 2021.
3. N. Konstantinidis, **A. Fos**, P. Švec, N. Papadopoulos, P. Vourna, E. Hristoforou. Morphology and magnetic properties of rapidly quenched Fe-B alloys. *Journal of Magnetism and Magnetic Materials*, 564. s. 2022.

### Conference proceedings

1. **A. Fos**, P. Švec, P. Švec, I. Janotová, D. Janičkovič, R. Tiwari, M. Búran. Effect of annealing on microstructure of rapidly quenched Fe-Sn-B based alloys. In J. Sitek, J. Vajda, I. Jamnický. *APCOM 2021*. Melville: AIP Publishing, 2021, ISBN 978-0-7354-4138-5.
2. P. Švec, I. Janotová, D. Janičkovič, I. Maťko, B. Butvinová, **A. Fos**, B. Kunca, M. Jergel, I. Škorvánek, M. Franko, Š. Luby, P. Švec. Rare-earth free nanocrystalline magnetics from rapidly quenched precursors. In Brunner, R. *SSSI 2020*. Bratislava: Comenius University, 2020, s. 96-98. ISBN 978-80-223-5018-1.
3. **A. Fos**, P. Švec, I. Janotová, D. Janičkovič, B. Butvinová, M. Búran, A. Kyritsi, N. Konstantinidis, J. Marcin, I. Škorvánek, P. Novák. Microstructure and magnetic properties of rapidly quenched Fe-Sn-B based alloys. *APCOM 2022*. Melville: AIP Publishing, 2023, ISBN 978-0-7354-4479-9.
4. B. Butvinová, P. Švec, **A. Fos**, I. Janotová, J. Škoviera, I. Maťko. Effect of short annealing on soft magnetic properties of Fe(Co)SnBP alloys. *APCOM 2022*. Melville: AIP Publishing, 2023, ISBN 978-0-7354-4479-9.